REPORT DOCUMENTATION PAGE

Form Approved
OMB NO. 0704-0188

1. AGENCY USE ONLY (Leave Blank)	2. REPORT DATE	3. REPORT TYPE AND DATES COVERED Final Report – 9/15/1997 – 2/1/2001

4. TITLE AND SUBTITLE
Photonic Crystal HIDE Materials Engineering

5. FUNDING NUMBERS
DAAG55-97-1-0366

6. AUTHOR(S)
L.C. Kimerling

7. PERFORMING ORGANIZATION NAME(S) AND ADDRESS(ES)
U.S. Army Research Office
P.O. Box 12211
Research Triangle Park, NC 27709-2211

8. PERFORMING ORGANIZATION REPORT NUMBER

9. SPONSORING / MONITORING AGENCY NAME(S) AND ADDRESS(ES)

U. S. Army Research Office
P.O. Box 12211
Research Triangle Park, NC 27709-2211

10. SPONSORING / MONITORING AGENCY REPORT NUMBER

37663.9-PH

11. SUPPLEMENTARY NOTES
The views, opinions and/or findings contained in this report are those of the author(s) and should not be construed as an official Department of the Army position, policy or decision, unless so designated by other documentation.

12 a. DISTRIBUTION / AVAILABILITY STATEMENT

Approved for public release; distribution unlimited.

12 b. DISTRIBUTION CODE

13. ABSTRACT (Maximum 200 words)

Milestone results have been achieved in the design, processing, and testing of dielectric and metallodielectric composite materials for the control of IR emissivity. Our theoretical analyses have shown that an omnidirectional reflectivity band can be produced with high dielectric contrast, multilayer structures. The theory was applied to design and fabricate a structure comprised of alternating Te and polymer layers that were produced by low cost evaporation and spin coating processes, respectively. These materials exhibit near perfect, omnidirectional reflectivity in the 8-12 mm range, and they can be easily fabricated for response within the 2-25 mm range. In the next term, we will develop a design foundation for materials selection and microstructural processing. We have developed a novel, low-cost process for the periodic placement of micron-dimensioned spheres and clusters of metal particles in two dimensional arrays. This process is the first example of stamping and filling a template with high precision at dimensions relevant to metallodielectric HIDE materials. A novel waveguide which utilizes the omnidirectional mirror to localize light in air was developed. This in turn led to the discovery of an optical coaxial waveguide which supports a TEM like mode in a a non-metalic structure.

14. SUBJECT TERMS
IR emissivity, omnidirectional reflectivity

15. NUMBER OF PAGES

16. PRICE CODE

17. SECURITY CLASSIFICATION OR REPORT UNCLASSIFIED	18. SECURITY CLASSIFICATION ON THIS PAGE UNCLASSIFIED	19. SECURITY CLASSIFICATION OF ABSTRACT UNCLASSIFIED	20. LIMITATION OF ABSTRACT UL

NSN 7540-01-280-5500

Standard Form 298 (Rev.2-89)
Prescribed by ANSI Std. 239-18
298-102

20030605 096

Statement of the problem studied

The problem studied pertained to the area of Highly-Controlled Infrared Dielectric Emissivity. In response to the military need for new low-cost IR materials. Novel composite materials, such as photonic crystals, whose electromagnetic properties can be fully engineered and manufactured by low-cost techniques were needed to be developed.

Summary of the most important results

The MIT Photonic Crystal HIDE Materials Engineering Team has achieved milestone results in designing, processing and testing dielectric and metallodielectric composite materials for control of IR emissivity. Our theoretical analyses have discovered that an omnidirectional reflectivity band can be produced with high dielectric contrast, multilayer structures, as discussed in detail in attachment #1. The theory was applied to design and fabricate a structure comprised of alternating Te and polymer layers that were produced by low cost evaporation and spin coating processes, respectively. These materials exhibit near perfect, omnidirectional reflectivity in the 8-12 μm range. This groundbreaking result has received international acclaim and was published in Science Magazine. The theoretical and experimental details of this 1-D omnidirectional reflector are presented in attachment # 2. We have also developed a novel, low-cost process for the periodic placement of micron-demensioned spheres and clusters of metal particles in two dimensional arrays, as detailed in attachment #3 and #4. This process is the first example of stamping and filling a template with high precision at dimensions relevant to metallodielectric HIDE materials. A sol-gel technique for producing multilayer dielectric films was developed and led to the fabrication of a nearly omnidirectional reflector corresponding to 1.55microns. This discovery is outlined in attachment #5. Our team used the omnidirectional mirror design criteria to develop a hollow all-dielectric waveguide for low-loss transmission of electromagnetic radiation. The design and experimental verification of this novel waveguide is described in attachment #6 This in turn has led to the development of a novel coaxial optical fiber which has been shown theoretically to support a TEM like mode similar to the one existing in metallic coaxial cables. This discovery was published in Science and is described in detail in attachment #7.

Publications and technical reports supported under this grant and contract

J. N. Winn, Y. Fink, S. Fan and J. D. Joannopoulos, *Omnidirectional reflection from a one- dimensional photonic crystal*, Optics Letters, **23**, No. 20, October 1998

Y. Fink, J. N. Winn, S. Fan, C. Chen, J. Michel and J. D. Joannopoulos, *A Dielectric Omnidirectional Reflector*, Science, **282**, November 1998

K. Chen, A. W. Sparks, H. C. Luan, D. R. Lim, K. Wada and L. C. Kimerling, *SiO2/TiO2 omnidirectional reflector and microcavity resonator via the sol-gel method,* Applied Physics Letters, **75**, No. 24, December 1999

Y. Fink, D. Ripin, S. Fan, C Chen, J. D. Joannopoulos and E. L. Thomas, *Guiding Optical Light in Air Using an All- Dielectric Structure*, Journal of Lightwave Technology, **17**, No. 11, November 1999

M. Ibanescu, Y. Fink, S. Fan, E. L. Thomas and J. D. Joannopoulos, *An All- Dielectric Coaxial Waveguide*, Science, **289**, July 2000

List of participating scientific personnel

Faculty

Linel C. Kimerling
Edwin L. Thomas
John D. Joannopoulos
Michael J. Cima

Other academic

Yoel Fink
Shanui Fan

Sponsored research staff

Jurgen Michel
Shanui Fan
Pirre Villeneuve

Research assistants

Desmond Lim
Augustine Urbas
Kevin Chin
Thomas Chen
Joseph Bernstein
Garry Maskaly
Ickwin Park
Joshua Winn

Report of Inventions
See attached receipt of Final Report of Inventions for HIDE program.

DEPARTMENT OF THE ARMY
U.S. ARMY ROBERT MORRIS ACQUISITION CENTER
RESEARCH TRIANGLE PARK CONTRACTING DIVISION
P.O. BOX 12211
RESEARCH TRIANGLE PARK, NC 27709-2211

6624100
MPC
PI - L. Kimerling

REPLY TO
ATTENTION OF   October 5, 2001

AMSSB-ACR 70-1t P-37663-PH

Subject: Research Agreement No. DAAG55-97-1-0366

Massachusetts Institute of Technology
Office of Sponsored Programs, Room E19-750
Cambridge, MA 02139-4307

Dear Administrator:

The period of performance of research under the subject agreement ended 14 Sep 2001. This office has initiated closing procedures for the agreement. The following reports and documents are required before this process can be completed.

Dept

<u>Final Technical Report</u>: A final technical report on the research is required to be delivered under the terms of the agreement by 14 Dec 2001. An original and two copies of reproducible quality must be mailed to the Army Research Office, ATTN: AMSRL-RO-BI (Technical Reports), P. O. Box 12211, Research Triangle Park, NC 27709-2211. The report must be shipped prepaid. The Army Research Office will not accept collect shipments. You are cautioned that failure to timely deliver the report may impact on the award of future agreements to your organization.

<u>Other Closing Documents</u>: The following documents must be submitted to your cognizant Office of Naval Research by 14 Dec 2001.

a. Final Report of Inventions **RECEIVED** contracts (DD Form 882).

Sent 7/6/01 → b. Final Financial Documents as required by the research agreement.

Sent 4/6/01 → c. Property Report.

Your cooperation in the timely submission of these reports will be appreciated. If there will be a delay in the submission of the reports, please advise both Government offices involved in the closeout of the agreement and provide an explanation of the reason for the delay. The closeout voice mail number for this office is 919-549-4340.

Sincerely,

Mary N. Jackson
Procurement Technician

Copy Furnished:

Office of Naval Research

XC: J. Bartels
For Follow-up
10/22/01
mm

Printed on Recycled Paper

Omnidirectional reflection from a one-dimensional photonic crystal

Joshua N. Winn, Yoel Fink, Shanhui Fan, and J. D. Joannopoulos

Massachusetts Institute of Technology, 77 Massachusetts Avenue, Cambridge, Massachusetts 02139

We demonstrate that one-dimensional photonic crystal structures (such as multilayer films) can exhibit complete reflection of radiation in a given frequency range for all incident angles and polarizations. We derive a general criterion for this behavior that does not require materials with very large indices. We perform numerical studies that illustrate this effect.   © 1998 Optical Society of America

OCIS codes: 230.4170, 230.1480.

Low-loss periodic dielectrics, or photonic crystals, allow the propagation of light to be controlled in otherwise difficult or impossible ways.[1-4] In particular, a photonic crystal can be a perfect mirror for light from any direction, with any polarization, within a specified frequency range.   It is natural to assume that a necessary condition for such omnidirectional reflection is that the crystal exhibit a complete three-dimensional photonic bandgap, that is, a frequency range within which there are no propagating solutions of Maxwell's equations. Here we report that this assumption is false—in fact a one-dimensional photonic crystal will suffice.   We introduce a general criterion for omnidirectional reflection for all polarizations and apply it to the case of a dielectric multilayer film.   Previous attempts to attain high reflectance for a wide range of incident angles involved dielectric films with high indices of refraction, high special dispersion properties, or multiple contiguous stacks of films.[5-9]

A one-dimensional photonic crystal has an index of refraction that is periodic in the y coordinate and consists of an endlessly repeating stack of dielectric slabs, which alternate in thickness from d_1 to d_2 and in index of refraction from n_1 to n_2. Incident light can be either s polarized ($\mathbf{E}$ is perpendicular to the plane of incidence) or p polarized (parallel). Because the medium is periodic in y and homogeneous in x and z, the electromagnetic modes can be characterized by a wave vector $\mathbf{k}$, with k_y restricted to $0 \leq k_y \leq \pi/a$. We may suppose that $k_z = 0$, $k_x \geq 0$, and $n_2 > n_1$ without loss of generality.   The allowed mode frequencies ω_n for each choice of $\mathbf{k}$ constitute the band structure of the crystal.   The continuous functions $\omega_n(\mathbf{k})$, for each n, are the photonic bands.

For an arbitrary direction of propagation, it is convenient to examine the projected band structure, which is shown in Fig. 1 for a quarter-wave stack with $n_1 = 1$ and $n_2 = 2$. To make this plot we first computed the bands $\omega_n(k_x, k_y)$ for the structure, using a numerical method to solve Maxwell's equations in a periodic medium.[10] (In fact, for the special case of a multilayer film, an analytic expression for the dispersion relation is available.[11]) Then, for each value of k_x, the mode frequencies ω_n for all possible values of k_y were plotted. Thus in the gray regions there are electromagnetic modes for some value of k_y, whereas in

the white regions there are no electromagnetic modes, regardless of k_y.

One obvious feature of Fig. 1 is that there is no complete bandgap. For any frequency there exists some electromagnetic mode with that frequency—the normal-incidence bandgap is crossed by modes with $k_x > 0$. This is a general feature of one-dimensional photonic crystals.

However, the absence of a complete bandgap does not preclude omnidirectional reflection. The criterion is not that there be no propagating states within the crystal; rather, the criterion is that there be no propagating states that can couple to an incident propagating wave. As we argue below, the latter criterion is equivalent to the existence of a frequency range in which the projected band structures of the crystal and the ambient medium have no overlap.

The electromagnetic modes in the ambient medium obey $\omega = c(k_x{}^2 + k_y{}^2)^{1/2}$, where c is the speed of light in the ambient medium, so generally $\omega > ck_x$. The whole region above the solid diagonal light lines $\omega = ck_x$ is filled with the projected bands of the ambient medium.

If a semi-infinite crystal occupies $y < 0$ and the ambient medium occupies $y > 0$, the system is no longer periodic in the y direction and the electromagnetic modes of the system can no longer be classified by a single value of k_y. These modes must be written as
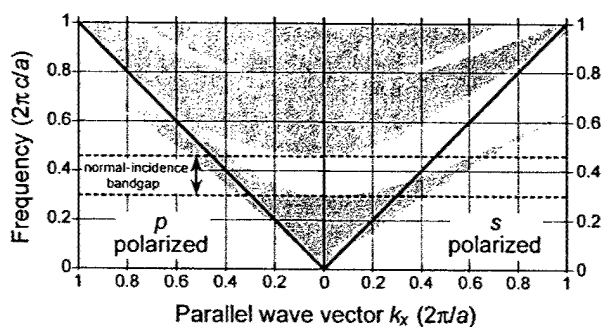

Fig. 1.   Projected band structure for a quarter-wave stack with $n_1 = 1$ and $n_2 = 2$.   Electromagnetic modes exist only in the shaded regions.   The s-polarized modes are plotted to the right of the origin, and the p-polarized to the left. The dark lines are the light lines $\omega = ck_x$. Frequencies are reported in units of $2\pi c/a$.

a weighted sum of plane waves with all possible k_y. However, k_x is still a valid symmetry label. The angle of incidence θ upon the interface at $y = 0$ is related to k_x by $\omega \sin \theta = ck_x$.

For there to be any transmission through the semi-infinite crystal at a particular frequency, there must be an electromagnetic mode available at that frequency that is extended for both $y > 0$ and $y < 0$. Such a mode must be present in the projected photonic band structures of both the crystal and the ambient medium. (The only states that could be present in the semi-infinite system that were not present in the bulk system are surface states, which decay exponentially in both directions away from the surface and are therefore irrelevant to the transmission of an external wave). Therefore, the criterion for omnidirectional reflection is that there exist a frequency zone in which the projected bands of the crystal have no states with $\omega > ck_x$.

In Fig. 1, the lowest two p bands cross at a point above the line $\omega = ck_x$, preventing the existence of such a frequency zone. This crossing occurs at the Brewster angle $\theta_B = \tan^{-1}(n_2/n_1)$, at which there is no reflection of p-polarized waves at any interface. At this angle there is no coupling between waves with k_y and $-k_y$, a fact that permits the band crossing to occur.

This difficulty vanishes when we lower the bands of the crystal relative to those of the ambient medium by raising the indices of refraction of the dielectric films. Figure 2 shows the projected band structure for the case $n_1 = 1.7$ and $n_2 = 3.4$. In this case there is a frequency zone in which the projected bands of the crystal and ambient medium do not overlap, namely, from the filled circle ($\omega a/2\pi c = 0.21$) to the open circle ($\omega a/2\pi c = 0.27$). This zone is bounded above by the normal-incidence bandgap and below by the intersection of the top of the first gray region for p-polarized waves with the light line.

Between the frequencies corresponding to the filled and open circles there will be total reflection from any incident angle for either polarization. For a finite number of films the transmitted light will diminish exponentially with the number of films. The calculated transmission spectra for a finite system of ten films (five periods) are plotted in Fig. 3 for various angles of incidence. The calculations were performed with transfer matrices.[12] The stop band shifts to higher frequencies with more-oblique angles, but there is a region of overlap that remains intact for all angles.

The graphic criterion for omnidirectional reflection is that the filled circle be lower than the open circle (the second band at $k_x = 0$, $k_y = \pi/a$). Symbolically,

$$\omega_{p1}\left(k_x = \frac{\omega_{p1}}{c}, k_y = \frac{\pi}{a}\right) < \omega_{p2}\left(k_x = 0, k_y = \frac{\pi}{a}\right),$$

(1)

where $\omega_{pn}(k_x, k_y)$ is the p-polarized band structure function for the multilayer film. Note that the left-hand side is a self-consistent solution for frequency ω_{p1}. The difference between these two frequencies is the range of omnidirectional reflection.

We calculated this range (when it exists) for a comprehensive set of film parameters. Since all the mode wavelengths scale linearly with $d_1 + d_2 = a$, we need consider only three parameters for a multilayer film: n_1, n_2, and d_1/a. To quantify the range of omnidirectional reflection (ω_1, ω_2) in a scale-independent manner, we report the range–midrange ratio, which is defined as $(\omega_2 - \omega_1)/\frac{1}{2}(\omega_2 + \omega_1)$.

For each choice of n_1 and n_2/n_1, there is a value of d_1/a that maximizes the range–midrange ratio. That choice can be computed numerically. Figure 4 is a contour plot of the ratio, as n_1 and n_2/n_1 are varied, for the maximizing value of d_1/a.

An approximate analytic expression for the optimal zone of omnidirectional reflection can be derived:

$$\frac{\Delta\omega}{2c} = \frac{a \cos\left(-\sqrt{\frac{A-2}{A+2}}\right)}{d_1 n_1 + d_2 n_2} - \frac{a \cos\left(-\sqrt{\frac{B-2}{B+2}}\right)}{d_1\sqrt{n_1^2 - 1} + d_2\sqrt{n_2^2 - 1}},$$
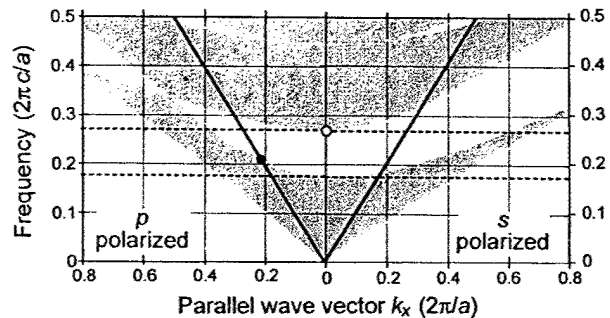
(2)

Fig. 2. Projected band structure for a quarter-wave stack with $n_1 = 1.7$ and $n_2 = 3.4$, with the same conventions as in Fig. 1.
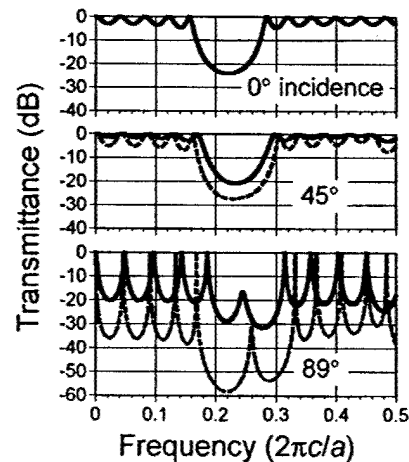

Fig. 3. Calculated transmission spectra for a quarter-wave stack of ten films ($n_1 = 1.7$, $n_2 = 3.4$) for three angles of incidence. Solid curves, p-polarized waves; dashed curves, s-polarized waves. The overlapping region of high reflectance (>20 dB) corresponds to the region between the open and filled circles of Fig. 2.
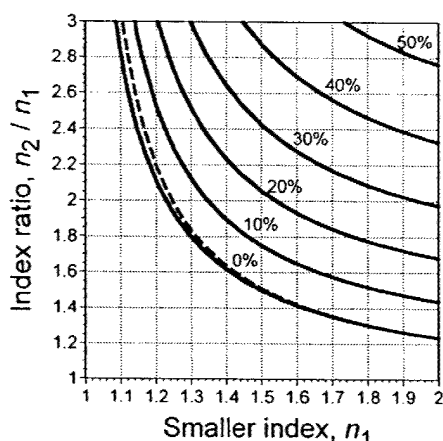
Fig. 4. Range–midrange ratio for omnidirectional reflection, plotted as contours. For the solid contours the optimal value of d_1/a was chosen. The dashed curve is the 0% contour for the case of a quarter-wave stack. For the general case of an ambient medium with index $n_0 \neq 1$, the abscissa becomes n_1/n_0.

where

$$A \equiv \frac{n_2}{n_1} + \frac{n_1}{n_2}, \qquad B \equiv \frac{n_2\sqrt{n_1{}^2 - 1}}{n_1\sqrt{n_2{}^2 - 1}} + \frac{n_1\sqrt{n_2{}^2 - 1}}{n_2\sqrt{n_1{}^2 - 1}}.$$

$$(3)$$

In deriving Eq. (2) we assumed that the optimal film is approximately a quarter-wave stack. Numerically we find this to be an excellent approximation for the entire range of parameters depicted in Fig. 4; the frequencies as predicted by this approximation are within 0.5% of the exact frequencies. As a result the optimization of d_1/a results in a range–midrange ratio very close to that which results from a quarter-wave stack with the same indices: $d_1/a = n_2/(n_2 + n_1)$. In Fig. 3, the 0% contour for quarter-wave stacks is plotted as a dashed curve, which is very close (always within 2% in the indices of refraction) to the numerically optimized contour.

It can be seen from Fig. 4 that, for omnidirectional reflection, the index ratio should be reasonably high (>1.5) and the indices themselves somewhat higher (by >1.5) than that of the ambient medium. The former condition increases the band splittings, and the latter depresses the frequency of the Brewster crossing. An increase in either factor can partially compensate for the other. The materials should also have a long absorption length for the frequency range of interest, especially at grazing angles, where the path length of the reflected light along the crystal surface is long.

Although we have illustrated our arguments by use of multilayer films, the notions in this Letter apply generally to any periodic dielectric function $n(y)$. What is required is the existence of a zone of frequencies in which the projected bands of the crystal and ambient medium have no overlap.

However, the absence of a complete bandgap does have physical consequences. In the frequency range of omnidirectional reflection there exist propagating solutions of Maxwell's equations, but they are states with $\omega < ck_x$ and decrease exponentially away from the crystal boundary. If such a state were launched from within the crystal, it would propagate to the boundary and reflect, just as in total internal reflection.

Likewise, although it might be arranged that the propagating states of the ambient medium do not couple to the propagating states of the crystal, any evanescent states in the ambient medium will couple to them. For this reason, a point source of waves placed very close ($d < \lambda$) to the crystal surface could indeed couple to the propagating state of the crystal. Such restrictions, however, apply only to a point source, and one can easily overcome them by simply adding a low-index cladding layer to separate the point source from the film surface.

References

1. E. Yablonovitch, Phys. Rev. Lett. **58**, 2059 (1987).
2. J. D. Joannopoulos, R. D. Meade, and J. N. Winn, *Photonic Crystals* (U. Princeton Press, Princeton, N.J., 1995).
3. J. Pendry, J. Mod. Opt. **41**, 209 (1994).
4. J. D. Joannopoulos, P. R. Villeneuve, and S. Fan, Nature (London) **386**, 143 (1997).
5. P. Baumeister, Opt. Acta **8**, 105 (1961).
6. J. D. Rancourt, *Optical Thin Films User Handbook* (SPIE Optical Engineering Press, Bellingham, Wash., 1996), pp. 68–71.
7. P. Yeh, *Optical Waves in Layered Media* (Wiley, New York, 1988), pp. 161–163.
8. K. V. Popov, J. A. Dobrowolski, A. V. Tikhonravov, and B. T. Sullivan, Appl. Opt. **36**, 2139 (1997).
9. M. H. MacDougal, H. Zhao, P. D. Dapkus, M. Ziari, and W. H. Steier, Electron. Lett. **30**, 1147 (1994).
10. R. D. Meade, A. M. Rappe, K. D. Brommer, and J. D. Joannopoulos, Phys. Rev. B **77**, 8434 (1993).
11. P. Yeh, A. Yariv, and C.-S. Hong, J. Opt. Soc. Am. **67**, 423 (1977).
12. E. Hecht, *Optics,* 2nd ed. (Addison-Wesley, Reading, Mass., 1987), pp. 373–378.

6. We used the same observed data as IPCC, updated (P. D. Jones, personal communication). For sources, see: N. Nicholls et al., in Climate Change 1995: The Science of Climate Change, J. T. Houghton et al., Eds. (Cambridge Univ. Press, Cambridge, 1996), pp. 133–192. Our analyses span 1881–1996. The conclusions of this paper do not depend on the precise start or end points.

7. We use data from two 1000-year unforced simulations with coupled ocean/atmosphere general circulation models: the Geophysical Fluid Dynamics Laboratory (GFDL) model [S. Manabe and R. J. Stouffer, J. Clim. 9, 376 (1996)]; and the U.K. Hadley Centre model (HadCM2) [S. F. B. Tett, T. C. Johns, J. F. B. Mitchell, Clim. Dyn. 13, 303 (1997)]. For the control-run results we used the full areal coverage to define the hemispheric means. For the observed data, coverage is incomplete and tends to increase with time. To test whether such coverage differences affected our results, we masked the control-run data with typical observed coverages and re-computed the correlations. The results were similar to the full-coverage results. Standard errors associated with the sample autocorrelations are typically of the order 0.05 or smaller in the case of the model data, and in the range 0.1 to 0.15 for the observational data. These were calculated by applying standard asymptotic formulae for the variance of sample autocorrelations [for example, see. p. 342 of W. A. Fuller, Introduction to Statistical Time Series, (Wiley-Interscience, ed. 2, New York, 1996)]. In doing so, we assume that the true autocorrelations used for calculating the theoretical results are those estimated from the model data. The result that the standard errors are larger for the observed series than the model series reflects the difference in sample sizes (116 against 1000). These results were also checked from the model data using a resampling procedure, based on the empirical standard deviation of sample autocorrelations calculated from maximally overlapping 116-year subseries of the 1000-year model runs; this produced results consistent with the asymptotic formulae. The results show that the difference between sample autocorrelations for the observed and either of the control-run series are 2 to 3 times the standard errors for the observed series. On this basis we conclude that the two sets of autocorrelations are indeed significantly different.

8. From HadCM2 [T. C. Johns et al., Clim. Dyn. 13, 103 (1997); J. F. B. Mitchell and T. C. Johns, J. Clim. 10, 245 (1997)]. In these simulations, which span the period 1861–2100, greenhouse-gas effects were modeled using observed CO_2 changes inflated to account for non-CO_2 greenhouse gases, and sulfate aerosol effects were modeled by using changes in surface albedo.

9. T. M. L. Wigley and S. C. B. Raper, Nature 357, 293 (1992); S. C. B. Raper, T. M. L. Wigley, R. A. Warrick, in Sea-Level Rise and Coastal Subsidence: Causes, Consequences and Strategies, J. D. Milliman and B. U. Haq, Eds. (Kluwer, Dordrecht, Netherlands, 1996), pp. 11–45. Simulations run from 1765 through 1996. The model differentiates between land and ocean in each hemisphere and gives hemispherically-specific temperature change results.

10. P. D. Jones, Clim. Mon. 17, 80 (1988); updated (P. D. Jones, personal communication).

11. Reviewed by C. K. Folland, T. R. Karl, K. Ya. Vinnikov, in Climate Change. The IPCC Scientific Assessment, J. T. Houghton, G. J. Jenkins, J. J. Ephraums, Eds. (Cambridge Univ. Press, Cambridge, 1990), pp. 195–238; C. K. Folland et al., in Climate Change 1992: The Supplementary Report to the IPCC Scientific Assessment, J. T. Houghton, B. A. Callander, S. K. Varney, Eds. (Cambridge Univ. Press, Cambridge, 1992), pp. 135–170; and by N. Nicholls et al. (6).

12. A. Kattenberg et al., in Climate Change 1995: The Science of Climate Change, J. T. Houghton et al., Eds. (Cambridge Univ. Press, Cambridge, 1996), pp. 285–357.

13. We have, nevertheless, tested this by subtracting estimated volcanic effects for all known major eruptions from the observed data. The influence on the autocorrelation structure is negligible.

14. D. V. Hoyt and K. H. Schatten, J. Geophys. Res. 98, 18895 (1994). Other reconstructions, such as by J. L. Lean, J. Beer, and R. Bradley [Geophys. Res. Lett. 22, 3195 (1995)], are similar. The results presented here do not depend on which solar data set is used.

15. The forcings used in the U-D model are the estimates employed by IPCC (12). Greenhouse gases included are CO_2, CH_4, N_2O, tropospheric and stratospheric ozone, and halocarbons. Aerosols included are the direct and indirect effects of sulfates and aerosols from biomass burning. Extensions beyond 1990 were made using the IS92a emissions scenario and observed CO_2 data. The IS92a scenario is the central "existing policies" scenario produced by IPCC in 1992 [J. A. Leggett, W. J. Pepper, R. J. Swart, in Climate Change 1992: The Supplementary Report to the IPCC Scientific Assessment, J. T. Houghton, B. A. Callander, S. K. Varney, Eds. (Cambridge Univ. Press, Cambridge, 1992), pp. 69–95]. The modifications made to this scenario are described in T. M. L. Wigley, Geophys. Res. Lett. 25, 2285 (1998).

16. The climate sensitivity (that is, the sensitivity to external forcing) is the equilibrium global-mean warming per unit radiative forcing, commonly expressed as the global-mean warming for a doubling of the CO_2 concentration, ΔT_{2x}. The most likely range for ΔT_{2x} is 1.5–4.5°C [J. F. B. Mitchell et al., in Climate Change. The IPCC Scientific Assessment, J. T. Houghton, G. J. Jenkins, J. J. Ephraums, Eds. (Cambridge Univ. Press, Cambridge, 1990), pp. 131–172] representing roughly the 90% confidence interval. The concept may be applied to any forcing. For example, the equilibrium global-mean warming for a 1% increase in solar irradiance (2.4 W/m^{-2}) would be 2.4($\Delta T_{2x}/\Delta Q_{2x}$) where ΔQ_{2x} is the forcing for 2x CO_2 (approx. 4 W/m^{-2}).

17. T. M. L. Wigley, P. D. Jones, S. C. B. Raper, Proc. Natl. Acad. Sci. U.S.A. 94, 8314 (1997). Note that these climate sensitivities depend on the assumed magni-

tudes of anthropogenic and solar forcing. In particular, they vary considerably if the magnitude of aerosol forcing is altered within the (large) uncertainty range of this component.

18. These values differ slightly from those in (17) because we use a different optimization interval.

19. We do this by fitting the U-D model (8) results for anthropogenic-plus-solar forcing to the observations (best-fit sensitivity 3.2°C) and then disaggregating the hemispheric-mean modeled temperatures into their solar, effective sulfate aerosol (see below), and residual anthropogenic components. The "effective aerosol" response is the sum of responses to direct and indirect sulfate aerosol forcing and tropospheric ozone. HadCM2 considers only direct sulfate aerosol forcing. Because its magnitude and pattern are similar to the effective aerosol forcing used in the U-D model, we considered the two to be equivalent for the purposes of producing adjusted-observed data.

20. Solar-plus-aerosol forcing leads to cooling. Thus, removing this component gives residuals with a larger positive trend than in the raw data.

21. G. A. Meehl, G. J. Boer, C. Covey, M. Latif, R. J. Stouffer, Eos 78, 445 (1997).

22. Supported by USDOE (T.M.L.W. and B.D.S.), NOAA (Award No. NA87GP0105 to T.M.L.W.) and NSF (DMS-9705166 to R.L.S.). Observed temperatures from P.D. Jones and D.E. Parker; control-run GCM data provided through the CMIP (21) project; SUL and GHG data provided by J.M. Gregory. NCAR is sponsored by the National Science Foundation.

16 September 1998; accepted 2 November 1998

A Dielectric Omnidirectional Reflector

Yoel Fink, Joshua N. Winn, Shanhui Fan, Chiping Chen, Jurgen Michel, John D. Joannopoulos, Edwin L. Thomas*

A design criterion that permits truly omnidirectional reflectivity for all polarizations of incident light over a wide selectable range of frequencies was used in fabricating an all-dielectric omnidirectional reflector consisting of multilayer films. The reflector was simply constructed as a stack of nine alternating micrometer-thick layers of polystyrene and tellurium and demonstrates omnidirectional reflection over the wavelength range from 10 to 15 micrometers. Because the omnidirectionality criterion is general, it can be used to design omnidirectional reflectors in many frequency ranges of interest. Potential uses depend on the geometry of the system. For example, coating of an enclosure will result in an optical cavity. A hollow tube will produce a low-loss, broadband waveguide, whereas a planar film could be used as an efficient radiative heat barrier or collector in thermoelectric devices.

Mirrors, probably the most prevalent of optical devices, are used for imaging and solar energy collection and in laser cavities. One can distinguish between two types of

Y. Fink, Department of Material Science and Engineering and Plasma Science and Fusion Center, Massachusetts Institute of Technology, Cambridge, MA 02139, USA. J. N. Winn, S. Fan, J. D. Joannopoulos, Department of Physics, Massachusetts Institute of Technology, Cambridge, MA 02139, USA. C. Chen, Plasma Science and Fusion Center, Massachusetts Institute of Technology, Cambridge, MA 02139, USA. J. Michel and E. L. Thomas, Department of Material Science and Engineering, Massachusetts Institute of Technology, Cambridge, MA 02139, USA.

*To whom correspondence should be addressed.

mirrors, the age-old metallic and the more recent dielectric. Metallic mirrors reflect light over a broad range of frequencies incident from arbitrary angles (that is, omnidirectional reflectance). However, at infrared and optical frequencies, a few percent of the incident power is typically lost because of absorption. Multilayer dielectric mirrors are used primarily to reflect a narrow range of frequencies incident from a particular angle or particular angular range. Unlike their metallic counterparts, dielectric reflectors can be extremely low loss. The ability to reflect light of arbitrary angle of incidence for all-dielectric structures has been associated with the existence of a

complete photonic band gap (*1–3*), which can exist only in a system with a dielectric function that is periodic along three orthogonal directions. In fact, a recent theoretical analysis predicted that a sufficient condition for the achievement of omnidirectional reflection in a periodic system with an interface is the existence of an overlapping band gap regime in phase space above the light cone of the ambient media (*4*). Now we extend the theoretical analysis and provide experimental realization of a multilayer omnidirectional reflector operable in infrared frequencies. The structure is made of thin layers of materials with different dielectric constants (polystyrene and tellurium) and combines characteristic features of both the metallic and dielectric mirrors. It offers metallic-like omnidirectional reflectivity together with frequency selectivity and low-loss behavior typical of multilayer dielectrics.

We consider a system that is made of an array of alternating dielectric layers coupled to a homogeneous medium, characterized by n_0 (such as air with $n_0 = 1$), at the interface. Electromagnetic waves are incident upon the multilayer film from the homogeneous medium. Although such a system has been analyzed extensively in the literature (*5–7*), the possibility of omnidirectional reflectivity was not recognized until recently. The generic system is described by the index of refraction profile in Fig. 1, where h_1 and h_2 are the layer thickness and n_1 and n_2 are the indices of refraction of the respective layers. The incident wave has a wave vector $\mathbf{k} = k_x \hat{e}_x + k_y \hat{e}_y$ and a frequency of $\omega = c|k|/n_0$, where c is the speed of light in vacuum and $\hat{e}_x$ and $\hat{e}_y$ are unit vectors in the x and y directions, respectively. The wave vector together with the normal to the periodic structure defines a mirror plane of symmetry that allows us to distinguish between two independent electromagnetic modes: transverse electric (TE) modes and transverse magnetic (TM) modes. For the TE mode, the electric field is perpendicular to the plane, as is the magnetic field for the TM mode. The distribution of the electric field of the TE mode (or the magnetic field in the TM mode) in a particular layer within the stratified structure can be written as a sum of two plane waves traveling in opposite directions. The amplitudes of the two plane waves in a particular layer α of one cell are related to the amplitudes in the same layer of an adjacent cell by a unitary 2 × 2 translation matrix $U^{(\alpha)}$ (*7*).

General features of the transport properties of the finite structure can be understood when the properties of the infinite structure are elucidated. In a structure with an infinite number of layers, translational symmetry along the direction perpendicular to the layers leads to Bloch wave solutions of the form

$$E_K(x,y) = E_K(x)e^{iKx}e^{ik_y y} \qquad (1)$$

where $E_K(x, y)$ is a field component, $E_K(x)$ is periodic, with a period of length a, and K is the Bloch wave number given by

$$K = \frac{i}{a}\ln\left(\frac{1}{2}\,\mathrm{Tr}(U^{(\alpha)})\right.$$
$$\left. \pm \left\{\frac{1}{4}\,[\mathrm{Tr}(U^{(\alpha)})]^2 - 1\right\}^{1/2}\right) \qquad (2)$$

Solutions of the infinite system can be propagating or evanescent, corresponding

Fig. 1. Schematic of the multilayer system showing the layer parameters (n_α and h_α are the index of refraction and thickness of layer α, respectively), the incident wave vector $\mathbf{k}$, and the electromagnetic mode convention. E and B are the electric and magnetic fields, respectively.
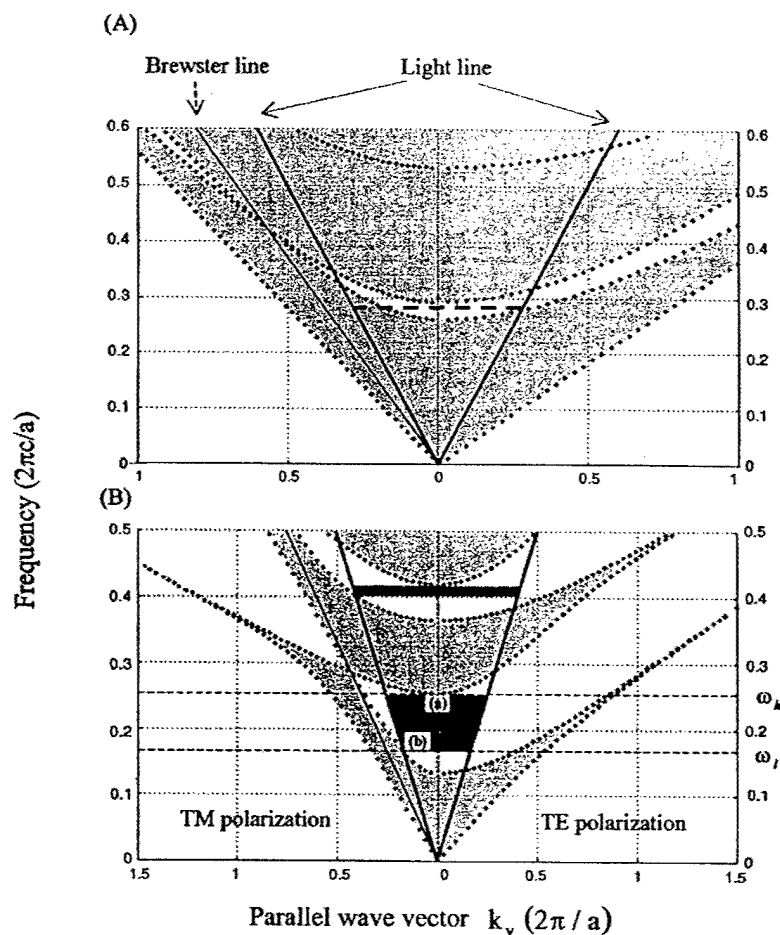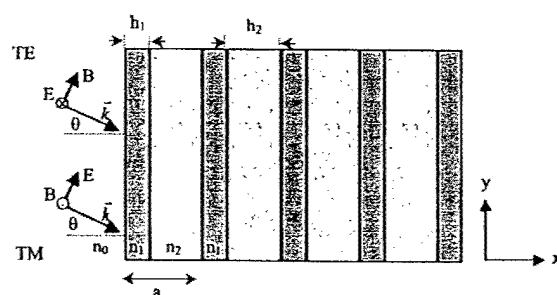

Fig. 2. **(A)** Projected band structure of a multilayer film with the light line and Brewster line, exhibiting a reflectivity range of limited angular acceptance with $n_0 = 1$, $n_1 = 2.2$ and $n_2 = 1.7$ and a thickness ratio of $h_2/h_1 = 2.2/1.7$. **(B)** Projected band structure of a multilayer film together with the light line and Brewster line, showing an omnidirectional reflectance range at the first and second harmonic. Propagating states, light gray; evanescent states, white; and omnidirectional reflectance range, dark gray. The film parameters are $n_1 = 4.6$ and $n_2 = 1.6$ with a thickness ratio of $h_2/h_1 = 1.6/0.8$. These parameters are similar to the actual polystyrene-tellurium film parameters measured in the experiment.

to real or imaginary Bloch wave numbers, respectively. The solution of Eq. 2 defines the band structure for the infinite system, $\omega(K, k_y)$. It is convenient to display the solutions of the infinite structure by projecting the $\omega(K, k_y)$ function onto the ω-k_y plane; Examples of such projected structures are shown in Fig. 2, A and B. The light gray areas highlight phase space where K is strictly real, that is, regions of propagating states, whereas the white areas represent regions containing evanescent states. The shape of the projected band structures for the multilayer film can be understood intuitively. At $k_y = 0$, the band gap for waves traveling normal to the layers is recovered. For $k_y > 0$, the bands curve upward in frequency. As $k_y \to \infty$, the modes become largely confined to the slabs with the high index of refraction and do not couple between layers (and are therefore independent of k_x).

For a finite structure, the translational symmetry in the directions parallel to the layers is preserved; hence, k_y remains a conserved quantity. In the direction perpendicular to the layers, the translational symmetry no longer exists. Nevertheless, the K number, as defined in Eq. 2, is still relevant, because it is determined purely by the dielectric and structural property of a single bilayer. In regions where K is imaginary, the electromagnetic field is strongly attenuated. As the number of layers is increased, the transmission coefficient decreases exponentially, whereas the reflectivity approaches unity.

Because we are primarily interested in waves originating from the homogeneous medium external to the periodic structure, we will focus only on the portion of phase space lying above the light line. Waves originating from the homogeneous medium satisfy the condition $\omega \geq ck_y/n_0$, where n_0 is the refractive index of the homogeneous medium, and therefore they must reside above the light line. States of the homogeneous medium with $k_y = 0$ are normal incident, and those lying on the $\omega = ck_y/n_0$ line with $k_x = 0$ are incident at an angle of 90°.

The states in Fig. 2A that are lying in the restricted phase space defined by the light line and that have a (ω, k_y) corresponding to the propagating solutions (gray areas) of the crystal can propagate in both the homogeneous medium and the structure. These waves will partially or entirely transmit through the film. Those states with (ω, k_y) in the evanescent regions (white areas) can propagate in the homogeneous medium but will decay in the crystal—waves corresponding to this portion of phase space will be reflected off the structure.

The multilayer system leading to Fig. 2A represents a structure with a limited reflectivity cone because for any frequency one can always find a k_y vector for which a wave at that frequency can propagate in the crystal and hence transmit through the film. For example, a wave with $\omega = 0.285 \times 2\pi c/a$ (dashed horizontal line in Fig. 2A) will be reflected for a range of k_y values ranging from 0 (normal incidence) to $0.285 \times 2\pi/a$ (90° incidence) in the TE mode, whereas in the TM mode it begins to transmit at a value of $k_y = 0.187 \times 2\pi/a$ (~41° incidence). The necessary and sufficient criterion (8) for omnidirectional reflectivity at a given frequency is that no transmitting state of the structure exists inside the light cone; this criterion is satisfied by frequency ranges marked in dark gray in Fig. 2B. In fact, the system leading to Fig. 2B exhibits two omnidirectional reflectivity ranges.

The omnidirectional range is defined from above by the normal incidence band edge $\omega_h(k_x = \pi/a, k_y = 0)$ (point a in Fig. 2B) and from below by the intersection of the top of the TM allowed band edge with the light line $\omega_l(k_x = \pi/a, k_y = \omega_l/c)$ (point b in Fig. 2B).

The exact expression for the band edges is

$$\frac{1 + \Lambda}{2} \cos(k_x^{(1)}h_1 + k_x^{(2)}h_2)$$

$$+ \frac{1 - \Lambda}{2} \cos(k_x^{(1)}h_1 - k_x^{(2)}h_2) + 1 = 0, \quad (3)$$

where $k_x^{(\alpha)} = \sqrt{(\omega n_\alpha/c)^2 - k_y^2}$ ($\alpha = 1, 2$) and

$$\Lambda \equiv \begin{cases} \dfrac{1}{2}\left(\dfrac{k_x^{(2)}}{k_x^{(1)}} + \dfrac{k_x^{(1)}}{k_x^{(2)}}\right) & \text{TE} \\[2ex] \dfrac{1}{2}\left(\dfrac{n_1^2 k_x^{(2)}}{n_2^2 k_x^{(1)}} + \dfrac{n_2^2 k_x^{(1)}}{n_1^2 k_x^{(2)}}\right) & \text{TM} \end{cases} \quad (4)$$

A dimensionless parameter used to quantify the extent of the omnidirectional range is the range to midrange ratio defined as $(\omega_h - \omega_l)/\frac{1}{2}(\omega_h + \omega_l)$. Figure 3 is a plot of this ratio as a function of n_2/n_1 and n_1/n_0, where ω_h and ω_l are determined by solutions of Eq. 3 with quarter wave layer thickness. The contours in this figure represent various equiomnidirectional ranges for different material index parameters and could be useful for design purposes.

It may also be useful to have an approximate analytical expression for the extent of the gap. This can be obtained by setting $\cos(k_x^{(1)}h_1 - k_x^{(2)}h_2) \cong 1$ in Eq. 3. We find that for a given incident angle θ_0, the approximate width in frequency is

$$\Delta\omega(\theta_0)$$

$$= \frac{2c}{h_1\sqrt{n_1^2 - n_0^2\sin^2\theta_0} + h_2\sqrt{n_2^2 - n_0^2\sin^2\theta_0}}$$

$$\times \left[\cos^{-1}\left(-\sqrt{\frac{\Lambda - 1}{\Lambda + 1}}\right) - \cos^{-1}\left(\sqrt{\frac{\Lambda - 1}{\Lambda + 1}}\right)\right]$$

$$(5)$$

At normal incidence, there is no distinction between TM and TE modes. At increasingly oblique angles, the gap of the TE mode increases, whereas the gap of the TM mode decreases. In addition, the center of the gap shifts to higher frequencies. Therefore, the
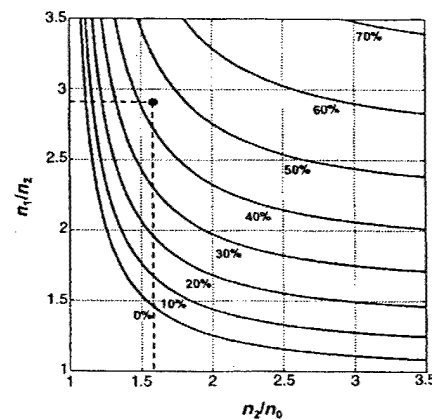

Fig. 3. (left). The range to midrange ratio $(\omega_h - \omega_l)/1/2(\omega_h + \omega_l)$, for the fundamental frequency range of omnidirectional reflection, plotted as contours. Here, the layers were set to quarter wave thickness and $n_1 > n_2$. The ratio for our materials is about 45% ($n_1/n_2 = 2.875$ and $n_2/n_0 = 1.6$). It is located at the intersection of the dashed lines (black dot).
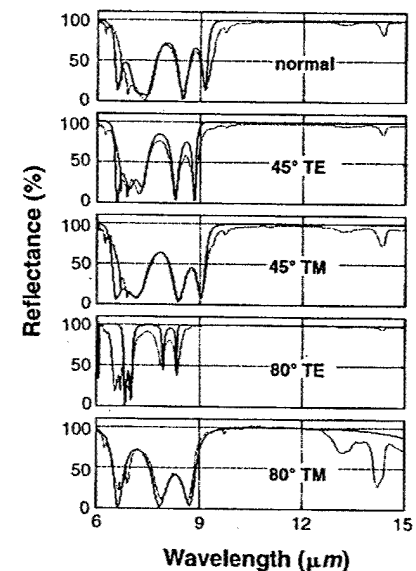

Fig. 4 (right). Calculated (solid line) and measured (dashed line) reflectance (in percent) as a function of wavelength for TM and TE modes at normal, 45°, and 80° angles of incidence, showing an omnidirectional reflectivity band.

criterion for the existence of omnidirectional reflectivity can be restated as the occurrence of a frequency overlap between the gap at normal incidence and the gap of the TM mode at 90°. Analytical expressions for the range to midrange ratio can be obtained by setting

$$\omega_h = \frac{2c}{h_2 n_2 + h_1 n_1} \cos^{-1}\left(-\left|\frac{n_1 - n_2}{n_1 + n_2}\right|\right)$$
(6a)

$$\omega_l = \frac{2c}{h_2\sqrt{n_2^2 - n_0^2} + h_1\sqrt{n_1^2 - n_0^2}}$$
$$\times \cos^{-1}\left(\left|\frac{n_1^2\sqrt{n_2^2 - n_0^2} - n_2^2\sqrt{n_1^2 - n_0^2}}{n_1^2\sqrt{n_2^2 - n_0^2} + n_2^2\sqrt{n_1^2 - n_0^2}}\right|\right)$$
(6b)

Moreover, the maximum range width is attained for thickness values that are not equal to the quarter wave stack although the increase in band width gained by deviating from the quarter wave stack is typically only a few percent (4).

In general, the TM mode defines the lower frequency edge of the omnidirectional range. An example can be seen in Fig. 2B for a particular choice of the indices of refraction. This can be proven by showing that

$$\left.\frac{\partial\omega}{\partial k_y}\right|_{TM} \geq \left.\frac{\partial\omega}{\partial k_y}\right|_{TE}$$
(7)

in the region that resides inside the light line. The physical reason for Eq. 7 lies in the vectorial nature of the electric field. In the upper portion of the first band, the electric field concentrates its energy in the high dielectric regions. Away from normal incidence, the electric field in the TM mode has a component in the direction of periodicity, and this component forces a larger portion of the electric field into the low dielectric regions. The group velocity of the TM mode is therefore enhanced. In contrast, the electric field of the TE mode is always perpendicular to the direction of periodicity and can concentrate its energy primarily in the high dielectric region.

A polystyrene-tellurium (PS-Te) materials system was chosen to demonstrate omnidirectional reflectivity. Tellurium has a high index of refraction and low loss characteristics in the frequency range of interest. In addition, its relatively low latent heat of condensation together with the high glass transi-

Table 1. Penetration depth (ξ) at different angles of incidence for the TE and TM modes.

Angle of incidence (degrees)	ξ_{TM} (μm)	ξ_{TE} (μm)
0	2.51	2.51
45	3.05	2.43
80	4.60	2.39

tion temperature of the PS minimizes diffusion of Te into the polymer layer. The choice of PS, which has a series of absorption peaks in the measurement range (9), demonstrates the competition between reflectivity and absorption that occurs when an absorption peak is located in the evanescent state region. The Te (0.8 μm) and PS (1.65 μm) films were deposited (10) sequentially to create a nine-layer film (11).

The optical response of this particular multilayer film was designed to have a high reflectivity region in the 10- to 15-μm range for any angle of incidence (in the experiment, we measure from 0° to 80°). The optical response at oblique angles of incidence was measured with a Fourier Transform Infrared Spectrometer (Nicolet 860) fitted with a polarizer (ZnS; SpectraTech) and an angular reflectivity stage (VeeMax; SpectraTech). At normal incidence, the reflectivity was measured with a Nicolet Infrared Microscope. A freshly evaporated aluminum mirror was used as a background for the reflectance measurements.

Good agreement between the calculated (12) and measured reflectance spectra at normal, 45°, and 80° incidence for the TM and TE modes is shown in Fig. 4. The regimes of high reflectivity at the different angles of incidence overlap, thus forming a reflective range of frequencies for light of any angle of incidence. The frequency location of the omnidirectional range is determined by the layer thickness and can be tuned to meet specifications. The range is calculated from Eq. 6 to be 5.6 μm, and the center wavelength is 12.4 μm, corresponding to a 45% range to midrange ratio shown in dashed lines in Fig. 3 for the experimental index of refraction parameters. These values are in agreement with the measured data. The calculations are for lossless media and therefore do not predict the PS absorption band at ~13 and 14 μm. The PS absorption peak is seen to increase at larger angles of incidence for the TM mode and to decrease for the TE mode. The physical basis for these phenomena lies in the relation between the penetration depth and the amount of absorption. The penetration depth is $\xi \propto \text{Im}(1/K)$, where K is the Bloch wave number. It can be shown that ξ is a monotonically increasing function of the incident angle for the TM mode of an omnidirectional reflector and is relatively constant for the TE mode. Thus, the TM mode penetrates deeper into the structure at increasing angles of incidence (Table 1) and is more readily absorbed. The magnitude of the imaginary part of the Bloch wave number for a mode lying in the gap is related to its distance from the band edges. This distance increases in the TE mode because of the widening of the gap at increasing angles of incidence and decreases in the TM mode because of the shrinking of the gap.

The PS-Te structure does not have a complete photonic band gap. Its omnidirectional reflectivity is due instead to the restricted phase space available to the propagating states of the system. The materials and processes were chosen for their low cost and applicability to large area coverage. The possibility of achieving omnidirectional reflectivity itself is not associated with any particular choice of materials and can be applied to many wavelengths of interest. Our structure offers metallic-like omnidirectional reflectivity for a wide range of frequencies and at the same time is of low loss. In addition, it allows the flexibility of frequency selection.

References and Notes
1. E. Yablonovitch, *Phys. Rev. Lett.* **58**, 2059 (1987).
2. S. John, *ibid.*, p. 2486.
3. J. D. Joannopoulos, R. Meade, J. N. Winn, *Photonic Crystals: Molding the Flow of Light* (Princeton Univ. Press, Princeton, NJ, 1995).
4. J. N. Winn et al., *Opt. Lett.*, **23**, 1573 (1998).
5. F. Abeles, *Ann. Phys.* **5**, 706 (1950).
6. M. Born and E. Wolf, *Principles of Optics* (Pergamon, ed. 6, 1980), p. 67.
7. P. Yeh et al., *J. Opt. Soc. Am.* **67**, 423 (1977).
8. A necessary condition for omnidirectional reflectivity is that light from outside the film cannot be allowed to access the Brewster angle $\theta_B = \tan^{-1}(n_1/n_2)$ of the multilayer structure because at this angle the TM mode will be transmitted through. This condition is met when the Brewster line lies outside of the light line or in terms of the refractive indices of the layers $\sin^{-1}(n_0/n_2) < \theta_B$. A sufficient condition is the existence of a particular frequency at which no propagating mode within the crystal exists between $k_y = 0$ and $k_y = n_0\,\omega/c$. Figure 2A is an example of a structure that does not have an omnidirectional reflectivity range even though its Brewster crossing is inaccessible to light coming from the homogeneous medium (the Brewster crossing lies outside the light cone). This is due to the large group velocity of modes in the lower band edge of the TM mode that allow every frequency to couple to a propagating state in the crystal. This should be contrasted with Fig. 2B, which exhibits an omnidirectional reflectivity range (highlighted in dark gray); the high indices of refraction actually allow for the opening of an additional omnidirectional reflectivity range in the higher harmonic as well.
9. C. J. Pouchert, *The Aldrich Library of FT-IR Spectra*, vol. II (Aldrich Chemical, Milwaukee, WI, 1985), p. 1204B.
10. A 0.8 ± 0.09-μm-thick layer of tellurium (99.99+%; Strem Chemicals) was vacuum evaporated at 10^{-6} torr and 7A (Ladd Industries 30000) onto a NaCl 25-mm salt substrate (polished NaCl window; Wilmad Glass). The layer thickness and deposition rate were monitored in situ with a crystal thickness monitor (Sycon STM100). A 10% solution of polystyrene (GoodYear PS standard, 110,000 g/mol) in toluene was spin cast at 1000 rpm onto the tellurium-coated substrate and allowed to dry for a few hours; the polymer layer thickness is 1.65 ± 0.09 μm.
11. The nine-layer film sequence was Te/PS/Te/PS/Te/PS/Te/PS/Te.
12. The calculations were done with the transfer matrix method described in (5) with the film parameters.
13. We thank J. F. Hester and A. Urbas for their valuable assistance and M. G. Bawendi and G. B. Kenney for stimulating discussions and inspiration. Supported in part by Defense Advanced Research Agency through U.S. Army Research Office under grant DAAG55-97-1-0366 and by the Air Force Office of Scientific Research under grants F49620-97-1-0325 and F49620-97-1-0385.

6 August 1998; accepted 6 October 1998

Particle arrays in micromolded substrates

Matthew E. Rosenthal, Malinda M. Tupper, and Michael J. Cima
Ceramic Processing Research Laboratory
Massachusetts Institute of Technology

Summary

Researchers at the Ceramics Processing Research Lab are investigating non-conventional methods of particle arrangement in an effort to create a photonic bandgap material. Experiments using silica spheres and copper particles placed in etched silicon substrates have been conducted which demonstrate the feasibility of precisely arranging particles. A micromolding technique developed at the CPRL shows promise in being able to precisely embed particles in a variety of materials.
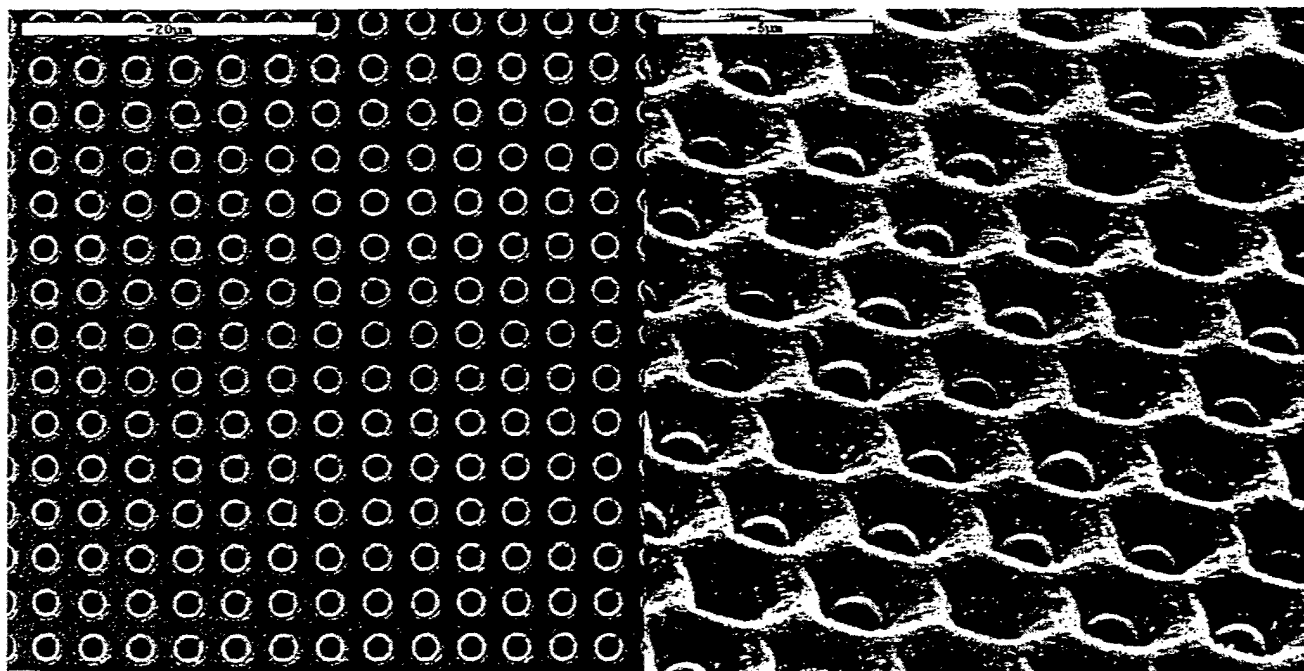
Figure 1a: Etched silicon substrate used as the master tool to form ordered arrays of holes in cheaper substrates such as plastic or wax.

Figure 1b: Glass spheres precisely ordered into hole array. The glass spheres are readily obtainable in very narrow size distributions and are used in this case to demonstrate the feasibility of the process. Metallized glass spheres or narrow size metal spheres will be used in the final composite

Experiments with monosized glass spheres

Experiments filling the holes with uniformly sized glass spheres have been very successful. A solution of ethanol and 1.58 μm silica standard spheres is applied to a silicon substrate with holes approximately 2 μm in diameter 3.5 μm apart. The substrate is sitting on a plate in a sonic bath to shake the particles into the holes. The particles settle into the holes, and the excess is wiped clean after the ethanol evaporates. Several applications result in complete filing of the matrix. Figure 1a is an SEM photograph of a silicon substrate, which can be used as a tool to mass produce matrices out of other materials such as wax or plastic. Figure 1b shows a completely filled array of glass spheres, demonstrating the feasibility of the concept of precisely arranging particles in an array. These encouraging results show promise for development of a system of reusable tooling able to capture and precisely arrange particles.

Experiments with wide size distribution metal particles

Experiments in filling arrays were also conducted using copper powder. The powder used has a wide size distribution, so many holes contain several particles while others only contain one (Figure 2). Improvements in powder processing are required to yield a more uniform ideal particle size of two microns in order to perfectly fill the holes. Ideally, a uniform particle size material would fill the lattice perfectly, as was demonstrated with the silica spheres.
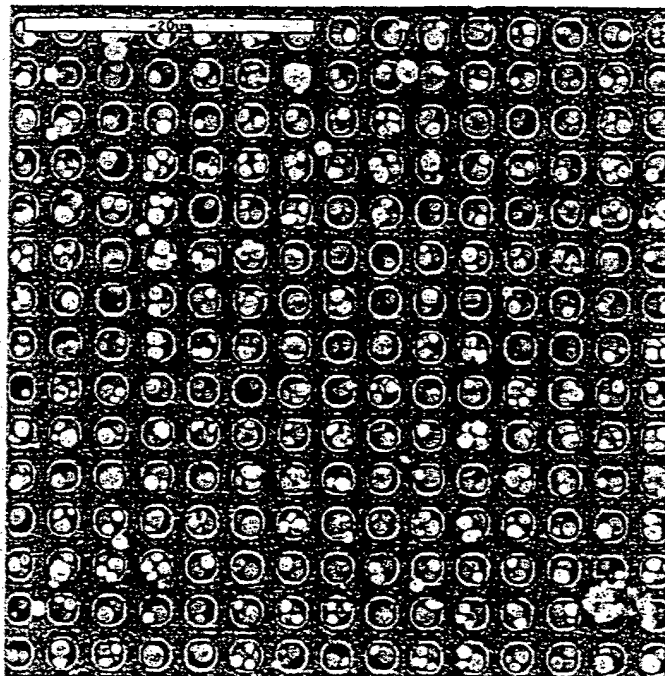
Figure 2: Silicon Substrate Filled With 1 μm Classified Copper Particles

Polymer substrates

A micromolding process can be used to transfer the pattern of holes to other materials. Preliminary experiments using paraffin have been conducted, although results indicate that paraffin is too soft a media to apply the particles too. Wiping of the substrate between applications damages the mold (Figure 3). Other materials such as epoxies and polyimides are being investigated as suitable molding materials. The ultimate goal is to create a thin film containing one layer of the lattice, and then to stack several films together to form a diamond lattice array.
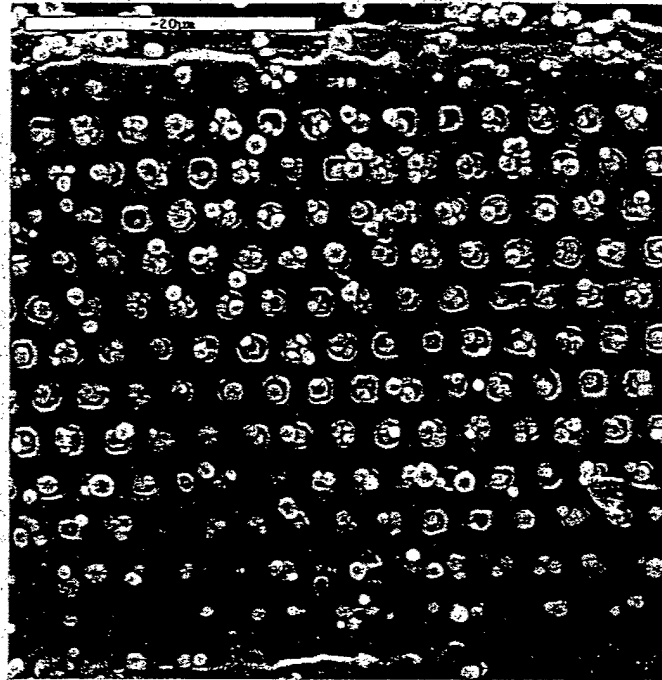
Figure 3: Wax Substrate With 1µm Copper Particles

Future work

Future work will consist of investigating different materials in which to place metallic particles, searching for a reliable source or method of production of uniform particle size particles, and examining the challenges involved in creating several layers of arranged particles to form a diamond lattice. Investigation into the feasibility of metallizing readily available uniformly sized particles, such as the glass spheres used in this work, will also be conducted. Current processing technology is unable to provide monosized metallic particles, and is considered a barrier to current research.

Metallodielectric Photonic Crystals

Collaborators: Shanhui Fan, Pierre Villenueve, Joshua Weitz, Matt Rosenthal,
Malinda Tupper, Michael Cima and John Joannopoulos

Using a finite difference time-domain method we studied the band structure of three-dimensional metallodielectric photonic crystals. Complete gaps are found in a diamond lattice of isolated metal spheres as well as for metal spheres embedded in a dielectric material like Teflon ($\varepsilon = 2.1$). The gap can be as large as 60% when the radius of spheres is approximately 21% of the cubic unit cell size.

Such optimal gaps require that spheres overlap across layers. We have, however, found a configuration which retains a large omnidirectional gap and can be fabricated in a layer-by-layer fashion. The band structure of this configuration using metal spheres with radii 17.7% of the cubic unit cell size is presented in the enclosed figure. The fabrication design is currently being implemented by Matt Rosenthal, Malinda Tupper and Michael Cima.

The unit cell size can be scaled depending on the wavelength of interest. For example, a diamond lattice with 4.95 µm unit cell size and non-overlapping metal spheres will have a 20% gap with a midgap frequency of 8.8 µm. To accommodate layer by layer growth the particles should be mono-dispersed with diameter 1.75 µm. Transmission calculations predict a 6 dB rejection per layer for isolated metal spheres.

We are also developing a finite difference time domain code that will model the dispersion relationships of more complicated materials. Using this method we have successfully calculated the dispersion curves of polariton and drude metals. Further testing is necessary to confirm that the simulations correctly model the time decay of propagating fields.

Band Structure for a Metallodielectric Photonic Crystal
Arranged in a Diamond Lattice with Non-Overlapping Metal Spheres

Collaborators: Shanhui Fan, Pierre Villeneuve, Joshua Weitz, Matt Rosenthal,
Malinda Tupper, Michael Cima, and John Joannopoulos
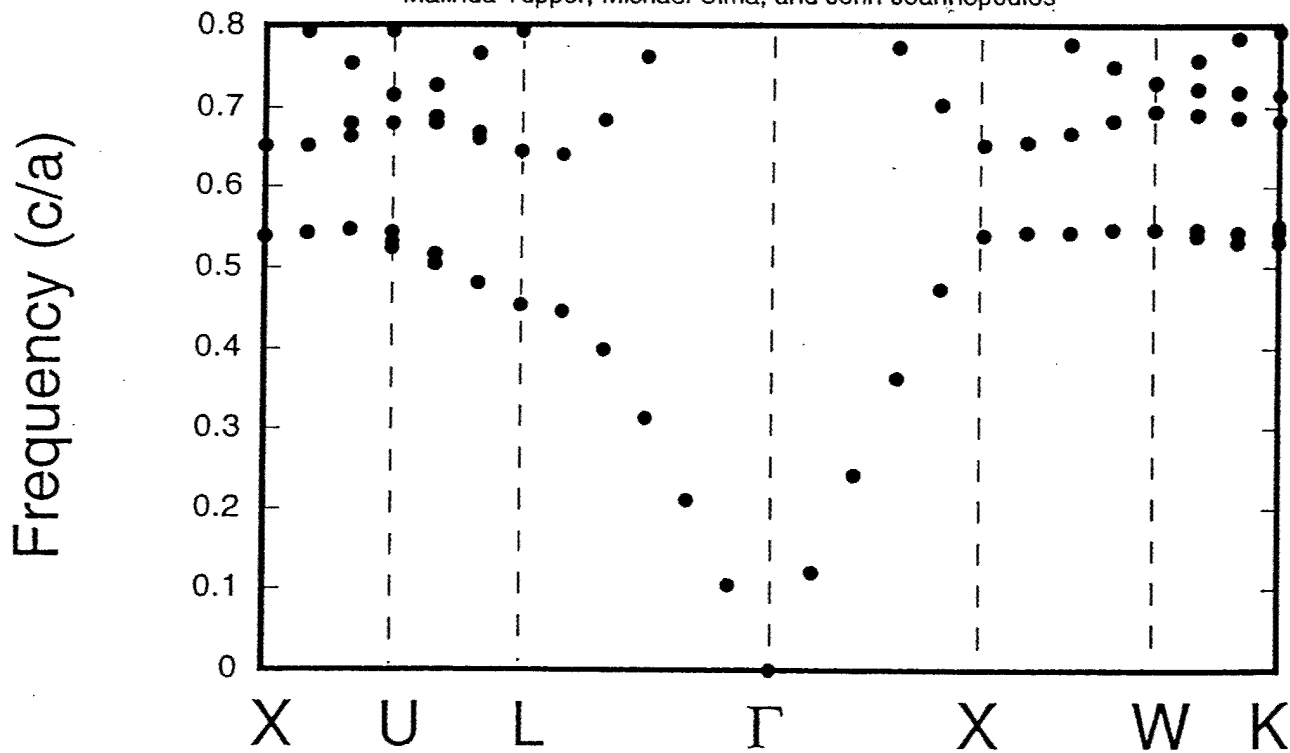
SiO$_2$/TiO$_2$ omnidirectional reflector and microcavity resonator via the sol-gel method

Kevin M. Chen, Andrew W. Sparks, Hsin-Chiao Luan, Desmond R. Lim, Kazumi Wada, and Lionel C. Kimerling[a]

Department of Materials Science and Engineering, Massachusetts Institute of Technology, Cambridge, Massachusetts 02139

Thin films of SiO$_2$ and TiO$_2$ were used to fabricate one-dimensional photonic crystal devices using the sol-gel method: an omnidirectional reflector and microcavity resonator. The reflector consisted of six SiO$_2$/TiO$_2$ bilayers, designed with a stopband in the near infrared. Reflectivity over an incident angle range of 0°–80° showed an omnidirectional band of 70 nm, which agrees with theoretical predictions for this materials system. The microcavity resonator consisted of a TiO$_2$ Fabry–Perot cavity sandwiched between two SiO$_2$/TiO$_2$ mirrors of three bilayers each. We have fabricated a microcavity with resonance at $\lambda = 1500$ nm and achieved a quality factor of $Q = 35$. We measured a resonance frequency modulation with a change in incident angle of light and defect layer thickness. © *1999 American Institute of Physics.* [S0003-6951(99)03850-4]

The fabrication techniques typically used for solid state microphotonic components are well suited for deposition onto wafer-sized surface areas. When deposition onto larger areas is required, other techniques that are better suited for macrophotonic applications may provide practical advantages. An example of such a technique is the sol-gel method.[1] The sol-gel method is an inexpensive wet-chemistry process that has been used in micro- and macro-photonic realms to deposit a variety of films onto various substrates as antireflection (AR) coatings,[1] selective filters,[2] Er-doped optical waveguides,[3] and Bragg grating waveguides.[4] The sol-gel method offers compositional flexibility over a range of oxides, piezoelectrics, and ferroelectrics.

This variety of materials makes it possible to explore the use of composite sol-gel structures as photonic band-gap devices. As optical analogs to semiconductors, photonic crystals possess a periodic refractive index that can give rise to bands of forbidden photon propagation states in the material.[5] With appropriate design, the presence of a defect in the periodic structure can introduce localized photonic states within the photonic band gap. Examples of one-dimensional photonic crystals are an omnidirectional reflector[6] and a waveguide microcavity.[7] Interference filters and microcavities fabricated from solid-state materials have been well-studied and characterized.

In this work, we demonstrate the feasibility of using the sol-gel method to fabricate one-dimensional photonic crystals with and without a defect—a microcavity and omnidirectional reflector, respectively—for macrophotonic applications. We choose SiO$_2$ and TiO$_2$ ($n_{\text{SiO}_2} = 1.47$, $n_{\text{TiO}_2} = 2.36$, measured at 632.8 nm) as a materials system with index contrast sufficiently large for omnidirectional reflectance.[6] The devices that we fabricate, because they are composed of oxides, may be well-suited for application in environments that see elevated temperatures, corrosion, and radiation.

In general, the sol-gel method begins with a step-polymerization process wherein an organometallic precursor is hydrolyzed to form a metal-oxide network gel. After deposition, typically via dip or spin coating, the solution is dried and fired to result in a final film with porosity as low as a few percent depending on the heat treatment.

Solutions of SiO$_2$ and TiO$_2$ were synthesized using recipes requiring minimal chemistry apparatus, following the methods given in Refs. 8 and 9, respectively. All chemical preparation was done in a glovebox filled with Ar atmosphere. Each solution was magnetically stirred overnight before use.

To deposit a thin film, several milliliters of solution were spin cast onto a cleaned Si wafer piece. The sample was then placed in a conventional tube furnace, dried at 100 °C for 2 min, and fired at 700 °C for 15 min. The film was allowed to cool to 200 °C for 10 min before removal from the furnace. Films of SiO$_2$ and TiO$_2$ received identical heat treatments.

For calibration, film thickness and refractive index were measured using a Gaertner Ellipsometer operating at 632.8 nm. Actual thicknesses were obtained via cross-sectional transmission electron microscopy (XTEM). Reflectance measurements were done using a Fourier transform infrared spectrometer (Nicolet 860; ~2 mm^2 beam spot size in normal incidence) with angle-dependence stage (SpectraTech Veemax; ~20 mm^2 spot size for 30°–80° off-normal) and ZnS polarizer (SpectraTech). Each measurement was referenced against an Au background.

The interference filter is composed of six bilayers of SiO$_2$ and TiO$_2$ quarter-wave films. The microcavity is composed of a half-wave TiO$_2$ "defect" layer sandwiched between mirrors consisting of three bilayers each. The XTEM micrographs of these devices show good thickness uniformity for individual films as well as the presence of interface and film defects (Fig. 1).

To reduce the thermal budget on the interference filter and microcavity devices, a minimum temperature for densification was desired. Single films of SiO$_2$ and TiO$_2$ fired at

---
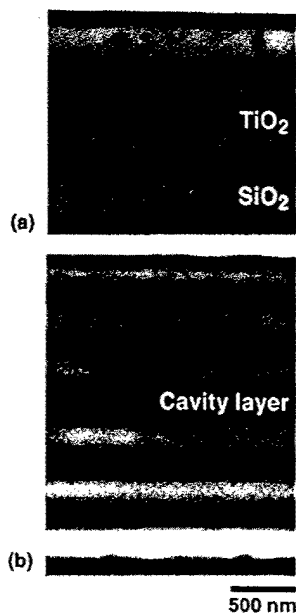[a]Electronic mail: lckim@mit.edu

Chen *et al.*

(a)

(b)

500 nm

FIG. 1. Cross-sectional TEM micrographs of devices fabricated by the sol-gel method: (a) omnidirectional reflector and (b) microcavity resonator. The micrographs detail films in the interior of the devices.
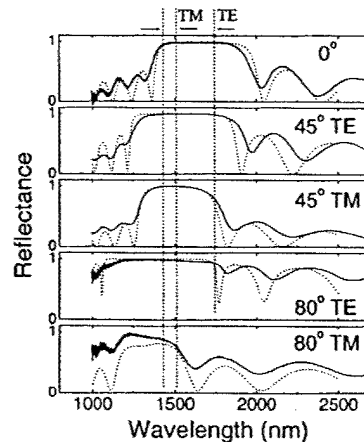

FIG. 2. Angle-dependent reflectance spectra of the omnidirectional reflector for TE and TM modes (dotted lines show calculated spectra). Omnidirectional reflection bands are marked by the dotted vertical lines.

500 °C contained macroscopic defects thought to be pores and cracks as shown by optical microscopy, which suggested incomplete densification. At 700 °C, these defects were not observed. Moreover, interference filters fabricated using 500 °C anneals showed considerably poorer reflectance spectra than those fabricated at 700 °C, presumably due to scattering from the defects and thickness irregularities. Therefore, 700 °C densification anneals were used for all devices.

The XTEM micrograph illustrates that the spin-coated films have good thickness uniformity and that the deposition process is repeatable. There is no stratification of film density due to the accumulation of heat treatments for initial films deposited in the multilayer, which would lead to an increase in refractive index[8] and appear as a nonuniformity in film thickness through a cross section. It can be concluded that the 15 min firing at 700 °C is sufficient for full densification of these films.

The angle-dependent reflectance plots for the interference filter are shown in Fig. 2. For the transverse electric (TE) and transverse magnetic (TM) polarizations, the reflectance bands shift to shorter wavelengths with increasing incident angle. The bandwidths, however, behave differently: the TE bandwidths increase while the TM bandwidths decrease with increasing incident angle. The reflectance behavior agrees with theoretical dispersion curves.[6,10] Using measured thicknesses and refractive indices for SiO_2 and TiO_2, we calculated theoretical angle-dependent reflectance spectra with the transfer matrix method.[10] In general, there is good agreement between the calculated and measured spectra.

Figure 2 shows that there is an overlapping reflectance band common to all spectra taken between the incident angles of 0°–80°; this is the omnidirectional reflectance band. For TE polarization, there is a 300 nm omnidirectional reflection band. For TM polarization there is a 70 nm band. The superposition of TE and TM polarizations results in a 70 nm band of omnidirectional reflectance for unpolarized incident light. These results are in good agreement with the predicted omnidirectional band[6] for this materials system, which is approximately 70 nm.

The ideal design for highest reflectance and sharpest reflectance band edges in an interference filter is a quarter-wave stack because Bragg interference among propagating waves within the structure is maximized. When film thicknesses are detuned from the quarter-wave optical thicknesses, as is the case here, Bragg interference is weakened and the filter exhibits a high reflectance range (HRR) sensitive to the average optical thickness of the layers in the filter.[11] Detuning can relax thickness constraints on individual layers while maintaining high reflectance over a wider range than achievable using quarter-wave thickness. The tradeoff is that there is a decrease in the maximum reflectance as well as a reduction in sharpness of the reflectance band edges. Applications requiring a wide HRR and process flexibility stand to benefit from detuning.

The reflectance spectra of a microcavity, on the other hand, is less forgiving to thickness and index variations. In a microcavity, the defect layer accommodates a resonant optical mode whose linewidth is determined by the reflectances of the adjacent mirrors. Since the cavity quality factor Q is sensitive to the mirror reflectances R_1 and R_2 as $Q \sim |\ln\sqrt{R_1 R_2}|^{-1}$ (for a lossless Fabry–Perot cavity), detuning in the mirror layers decreases Q by increasing leakage of the confined mode. Thus by measuring Q, we obtain a direct indication of the thickness and index accuracy of films deposited by the sol-gel method.

Angle-dependent reflectance plots for the microcavity are shown in Fig. 3. In normal incidence, the cavity resonance occurs at $\lambda = 1500$ nm and a highest quality factor of $Q = 35$ was measured. By comparison, solid-state vacuum deposition techniques can be used to fabricate microcavities with $Q \sim 10\,000$. Figure 1(b) illustrates that film thicknesses for the microcavity showed more variations than seen in the interference filter. The low Q indicates that the deposition procedure requires finer control for increased layer-to-layer thickness uniformity.

Cavity Q is also sensitive to absorption. The calculated spectrum shown in Fig. 3 was obtained using the measured thicknesses and indices and an approximated complex di-

Attachment 5 (page 3)

Appl. Phys. Lett., Vol. 75, No. 24, 13 December 1999
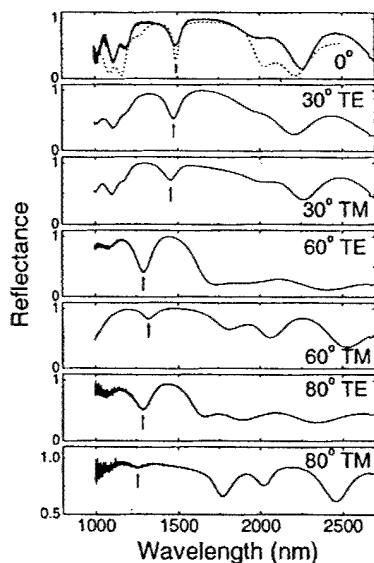
Chen *et al.*   3807

FIG. 3. Angle-dependent reflectance spectra of the microcavity resonator for TE and TM modes. A calculated spectrum is shown for normal incidence (dotted line). The arrows indicate cavity resonant frequency.

FIG. 4. Normal incidence spectra for microcavities with different defect layer thicknesses t_{defect}. The arrows indicate cavity resonant frequency: for $\lambda = 1400$ nm, $t_{\text{defect}} = 210$ nm; for $\lambda = 1500$ nm, $t_{\text{defect}} = 270$ nm.

electric constant ϵ''. The fit was found using $\epsilon'' = 0.04$, which is reasonable under the assumption that the absorption coefficient $\alpha = (\lambda Q)^{-1}$, where λ is the cavity resonant frequency, so that $\epsilon'' = 2n_{\text{TiO}_2}n''_{\text{TiO}_2} = 2n_{\text{TiO}_2}(\alpha\lambda/2\pi) = (n_{\text{TiO}_2})/\pi Q \approx 0.02$.

The resonance behavior is dependent on incident angle. For TE polarization, the resonance deepens with increasing incident angle; for TM polarization, it is progressively reduced. This behavior is understood in light of the reflectance bandwidths for the interference filter: the increasing bandwidth for TE modes leads to improved confinement of the resonance at higher angles, and vice versa for the TM modes. Increasing the angle of incidence also shifts the resonant frequency to shorter wavelengths. The resonance tuning may be useful for modulation of signals. The cavity resonance is also tuned by the defect layer thickness. Normal incidence spectra for microcavities with different cavity thicknesses are shown in Fig. 4.

On each device, surface defects such as flakes and cracks could be seen via optical microscopy. Regions of delamination both from the substrate and from the uppermost layers were also seen by XTEM. These defects are thought to be due to the buildup of internal stresses induced by the cyclic anneals since the ratio of thermal expansion coefficients is $\alpha_{\text{SiO}_2}/\alpha_{\text{TiO}_2} \approx 1.58$ at $700\,°\text{C}$.[12] Additionally, the high heating rate corresponds to film shrinkage on the order of 40%,[13] which can induce significant film strain. Improvements to the structural integrity of the final devices include the following: a reduction of thermal cycling via alternative annealing techniques, and the inclusion of adhesion or accommodation layers at the substrate and within the multilayer. Another effect of uneven surface topology is its contribution towards increasing the film thickness variation for subsequent layers.
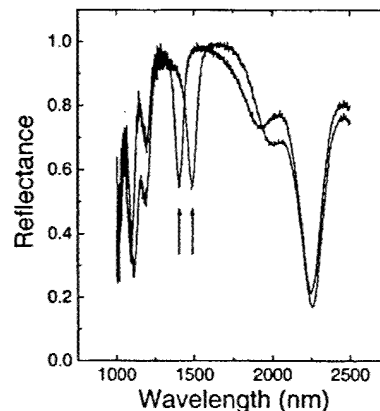
Clearly, a highly controlled deposition and annealing process is necessary to reduce surface roughness. Despite the presence of surface defects, our sol-gel interference filters are shown to be sufficient for applications that require high reflectance over a large surface area.

In summary, we have fabricated via the sol-gel method an omnidirectional reflector using SiO_2 and TiO_2 thin films. Using the same materials, we have demonstrated a microcavity with resonance at $\lambda = 1500$ nm. We show that the resonance is modulated by the incident angle of light and the defect layer thickness. The tolerance of reflectance to detuning enables the sol-gel method to be used for fabrication of omnidirectional reflectors. The technique must be highly controlled for fabrication of high Q microcavities.

[1] C. J. Brinker and G. W. Scherer, *Sol-Gel Science: The Physics and Chemistry of Sol-Gel Processing* (Academic, New York, 1990); L. F. Francis, Mater. Manuf. Processes **12**, 963 (1997).

[2] P. K. Biswas, D. Kundu, and D. Ganguli, J. Mater. Sci. Lett. **6**, 1481 (1987).

[3] A. Bahtat, M. Bouazaoui, B. Mahtat, and J. Mugnier, Opt. Commun. **111**, 55 (1994).

[4] M. A. Fardad, H. Luo, Y. Beregovski, and M. Fallahi, Opt. Lett. **24**, 460 (1999).

[5] J. D. Joannopoulos, R. Meade, and J. N. Winn, *Photonic Crystals: Molding the Flow of Light* (Princeton University Press, Princeton, NJ, 1995).

[6] Y. Fink, J. N. Winn, S. Fan, C. Chen, J. Michel, J. D. Joannopoulos, and E. L. Thomas, Science **282**, 1679 (1998).

[7] J. S. Foresi, P. R. Villeneuve, J. Ferrera, E. R. Thoen, G. Steinmeyer, S. Fan, J. D. Joannopoulos, L. C. Kimerling, H. I. Smith, and E. P. Ippen, Nature (London) **390**, 143 (1997).

[8] B. D. Fabes, D. P. Birnie III, and B. J. J. Zelinski, Thin Solid Films **254**, 175 (1995).

[9] U. Selvaraj, A. V. Prasadarao, S. Komarneni, and R. Roy, J. Am. Ceram. Soc. **75**, 1167 (1992).

[10] P. Yeh, *Optical Waves in Layered Media* (Wiley, New York, 1988), p. 126.

[11] H. Li, G. Gu, H. Chen, and S. Zhu, Appl. Phys. Lett. **74**, 3260 (1999).

[12] D. N. Nikogosyan, *Properties of Optical and Laser-Related Materials: A Handbook* (Wiley, Chichester, 1997), pp. 155 and 268.

[13] J. L. Keddie, P. V. Braun, and E. P. Giannelis, J. Am. Ceram. Soc. **77**, 1592 (1994).

Guiding Optical Light in Air Using an All-Dielectric Structure

Yoel Fink, Daniel J. Ripin, Shanhui Fan, Chiping Chen, John D. Joannopoulos, and Edwin L. Thomas

Abstract—The emergence of a dielectric omnidirectional multilayer structure [1]–[4] opens new opportunities for low loss broad-band guiding of light in air. We demonstrate the effectiveness of such an approach by fabricating a broad-band, low-loss hollow waveguide in the 10-μm region and measuring its transmission around a 90° bend. The generality of the solution enables the application of the method to many wavelengths of interest important in telecommunication applications as well as for guiding high-power lasers in medical and other fields of use.

Index Terms— Dielectric, high-power lasers, hollow wavegusides, light conduits, low-loss broad-band transmission, medical lasers, multimode waveguide, omnidirectional reflectors, optical fibers, optical confinement, single-mode waveguide.

I. INTRODUCTION

GUIDING light in dielectric fibers has had a tremendous impact on many aspects of our life—we rely on fiber optics for communications as well as for illumination and a host of medical applications. The typical optical fiber has a high index core and a low index cladding such that the light is confined to the core by total internal reflection. Two inherent drawbacks exist in this approach: the first is absorption. Since the light is traveling through a dense medium for long distances, material absorption becomes significant even in low loss materials. To compensate for losses the fiber is doped with erbium which is used to amplify the signal. This in turn limits the bandwidth of the fiber to that of the narrow erbium excitation lines. The other weakness follows from the confinement mechanism—total internal reflection which confines light only of a limited angle. Conventional optical fibers cannot guide light around sharp turns, which is especially important in optical integrated circuits. Light guided in a hollow waveguide lined with an omnidirectional reflecting film propagates primarily through air and will therefore have substantially lower absorption losses. In addition, the confine-

ment mechanism does not have angular dependence allowing for guiding light around sharp bends with little or no leakage.

Most hollow waveguides fabricated to date [5]–[7], have internal metallic and dielectric layers. It has been shown [8] that the addition of dielectric layers to a metallic waveguide could lower the losses significantly. In contrast, our system is an all dielectric waveguide which confines all frequencies contained in its omnidirectional range. In principle this type of structure can have lower losses than the combined metal and dielectric structure since the waves do not interact with a lossy metallic layer. Although our proof of concept demonstration involves a large diameter multimode waveguide, one can fabricate a much smaller tube that could in principle be made to support a single mode.

II. PRINCIPLE OF OPERATION

A schematic of the hollow tube is presented in Fig. 1, as well as the index of refraction profile. In a realistic light guiding scenario involving many bends there exist no global symmetries and thus one cannot distinguish between independent TE and TM modes. Locally one can define a plane of incidence with respect to the normal to the film surface and the incident wave vector. Light entering into such a tube will invariably hit the walls many times and explore a wide range of angle of incidence of both polarizations with respect to any local plane of incidence. Since the air region is bounded by a structure that has a gap which encompasses all angles and polarizations the wave will be reflected back into the tube and will propagate along the hollow core as long as $k_z \neq 0$.

III. SAMPLE PREPARATION PROCEDURE

A Drummond 1.92 mm o.d. silica glass capillary tube was cleaned in concentrated sulfuric acid. The first tellurium layer was thermally evaporated using a LADD 30 000 evaporator fitted with a Sycon Instruments STM100 film thickness monitor. The capillary tube was axially rotated to ensure uniformity during coating. The first polymer layer was deposited by dip coating the capillary tube in a solution of 5.7 g polystyrene DOW 615APR in 90 g toluene. The next layer is tellurium deposited in the same method outlined above. The subsequent polymer layers are made of polyurethane diluted in mineral spirits. The device has a total of nine layers, five Te and four polymer and a total length of 10 cm. The layer thickness are approximately 0.8 μm for the tellurium layer (refractive index 4.6) and 1.6 μm for the polystyrene layer (refractive index 1.59). An optimal design will vary the layer thickness according to the zeros of the Bessel functions. Performance as

Y. Fink is with the Department of Materials Science and the Plasma Science and Fusion Center, Massachusetts Institute of Technology, Cambridge, MA 02139 USA (e-mail: yoel@mit.edu).

D. J. Ripin, S. Fan, and J. D. Joannopoulos are with the Department of Physics, Massachusetts Institute of Technology, Cambridge, MA 02139 USA (e-mail: shanhfan@mit.edu).

C. Chen is with the Plasma Science and Fusion Center, Massachusetts Institute of Technology, Cambridge, MA 02139 USA.

E. L. Thomas is with the Department of Materials Science, Massachusetts Institute of Technology, Cambridge, MA 02139 USA (e-mail: elt@mit.edu).

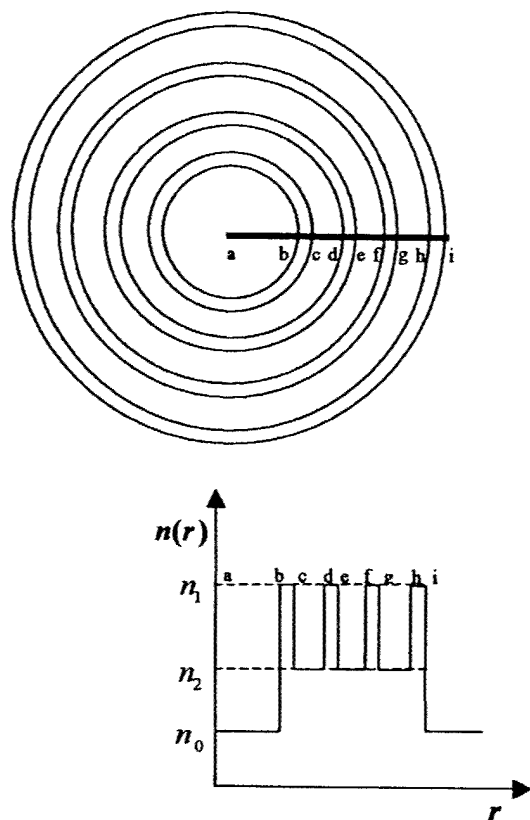Publisher Item Identifier S 0733-8724(99)08813-1.

Fig. 1. Cross section of the hollow waveguide showing the hollow core and the dielectric films, also shown is the index of refraction profile in the radial direction.
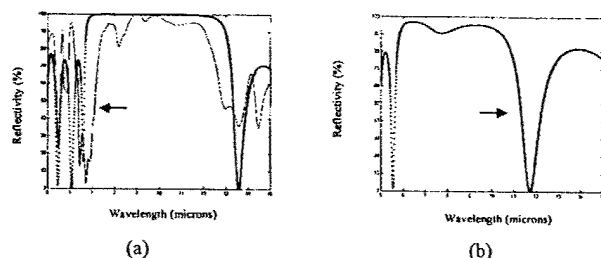

Fig. 2. (a) Measured (dashed) and calculated (dots) normal incidence reflectance for hollow waveguide in the radial direction. (b) Calculated grazing incidence reflectance for the TM mode.

well as the layer thickness were monitored by IR spectroscopy. The reflectivity of the deposited structure was measured in the radial direction using a Nicolet FTIR microscope and a variable size aperture, to ensure domination by radial reflection. The coated capillary tube was then inserted in a heat shrink tube which was filled with silicone rubber. Finally, the glass tube was dissolved using concentrated hydrofluoric acid (48%). The resulting hollow tube assembly is thus lined with the mirror coating and is both flexible and mechanically stable.

IV. RESULTS AND DISCUSSION

The reflectance measurements and simulations are shown for normal incidence in Fig. 2(a). The measured gap width is smaller than predicted, probably due to microdefects in the Te
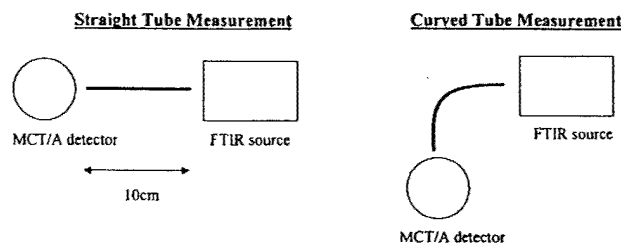

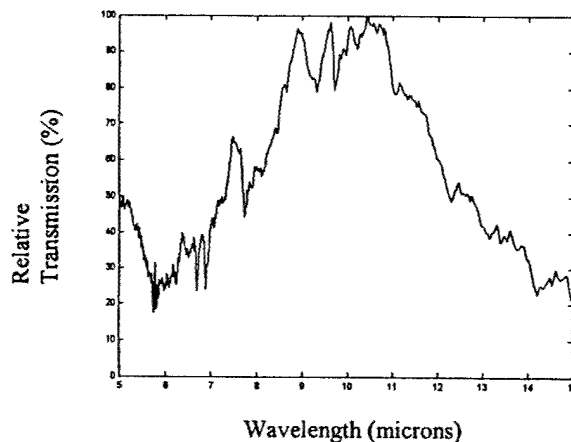Fig. 3. Hollow tube transmission measurement setup on the spectrophotometer (FTIR).

Fig. 4. Transmission through the hollow waveguide around a 90° bend as a function of wavelength.

layers. In addition there are absorption (8 μm) peaks due to the polyurethane. Fig. 2(b) is the calculation of the reflectance at grazing incidence for the TM mode. Since the omnidirectional frequency range is defined from above (high frequency edge) by the normal incidence gap edge (arrow) and from below by the grazing incidence gap edge (arrow) the extent of the gap is completely defined by these two data points. The extent of the omnidirectional range for the parameters used in this experiment is approximately 40% [1], [2].

The transmission through the tube was measured using a Nicolet Magna 860 FTIR bench with an MCT/A detector. The transmission was measured around a 90° bend at a radius of curvature of approximately 1 cm, which was compared, to the straight tube transmission to correct for entrance and exit effects. A schematic of the measurement layout is presented in Fig. 3.

The results shown in Fig. 4 indicate a high transmission around the 90° bend for a spectral band that corresponds to the omnidirectional gap. The relatively high noise level in the measurement is due to the lack of purge. This measurement provides a proof-of-concept indicating the low loss characteristics and guiding abilities of the all dielectric hollow waveguide.

ACKNOWLEDGMENT

REFERENCES

[1] J. N. Winn, Y. Fink, S. Fan, and J. D. Joannopoulos, "Omnidirectional reflection from a one-dimensional photonic crystal," *Opt. Lett.*, vol. 23, no. 20, pp. 1573–1575, 1998.

[2] Y. Fink, J. N. Winn, S. Fan, J. Michel, C. Chen, J. D. Joannopoulos, and E. L. Thomas, "An omnidirectional dielectric reflector," *Science*, vol. 282, pp. 1679–1682, 1998.

[3] D. N. Chigrin, A. V. Lavvrinenko, D. A. Yarotsky, and S. V. Gaponenko, "Observation of total omnidirectional reflection from a one-dimensional dielectric lattice," *Appl. Phy. A*, vol. 68, pp. 25–28, 1999.

[4] P. S. J. Russell, S. Tredwell, and P. J. Roberts, "Full photonic bandgaps and spontaneous emission control in 1D multilayer dielectric structures," *Opt. Commun.*, vol. 160, no. 1–3, pp. 66–71, 1999.

[5] M. Miyagi, A. Hongo, Y. Aizawa, and S. Kawakami, "Fabrication of germanium-coated nickel hollow waveguides for infrared transmission," *Appl. Phys. Lett.*, vol. 43, pp. 430–432, 1983.

[6] N. Croitoru, J. Dror, and I. Gannot, "Characterization of hollow fibers for the transmission of infrared radiation," *Appl. Opt.*, vol. 29, pp. 1805–1809, 1990.

[7] Y. Matsuura and J. Harrington, "Hollow glass waveguides with three-layer dielectric coating fabricated by chemical vapor deposition," *J. Opt. Soc. Amer.*, vol. 14, no. 6, 1997.

[8] M. Miyagi and S. Kawakami, "Design theory of dielectric coated circular metallic waveguides for infrared transmission," *J. Lightwave Technol.*, vol. LT-2, pp. 116–126, 1984.

[9] P. Yeh, A. Yariv, and E. Marom, "Theory of a Bragg fiber," *J. Opt. Soc. Amer.*, vol. 68, no. 9, 1978.

Daniel J. Ripin, photograph and biography not available at the time of publication.

Shanhui Fan, photograph and biography not available at the time of publication.

Chiping Chen, photograph and biography not available at the time of publication.

John D. Joannopoulos, photograph and biography not available at the time of publication.

Edwin L. Thomas, photograph and biography not available at the time of publication.

Yoel Fink, photograph and biography not available at the time of publication.

An All-Dielectric Coaxial Waveguide

M. Ibanescu,[1] Y. Fink,[2] S. Fan,[1] E. L. Thomas,[2]
J. D. Joannopoulos[1]

An all-dielectric coaxial waveguide that can overcome problems of polarization rotation and pulse broadening in the transmission of optical light is presented here. It consists of a coaxial waveguiding region with a low index of refraction, bounded by two cylindrical, dielectric, multilayer, omnidirectional reflecting mirrors. The waveguide can be designed to support a single mode whose properties are very similar to the unique transverse electromagnetic mode of a traditional metallic coaxial cable. The new mode has radial symmetry and a point of zero dispersion. Moreover, because the light is not confined by total internal reflection, the waveguide can guide light around very sharp corners.

Waveguides are the backbone of modern optoelectronics and telecommunications systems. There are currently two major, and very distinct, types of waveguides (metallic and dielectric) that are used in two separate regimes of the electromagnetic spectrum. For radio frequencies, the metallic coaxial cable is of greatest prominence (1). In this type of cable, the entire electromagnetic field is confined between two coaxial metal cylinders. The important fundamental electromagnetic mode of a coaxial cable is the transverse electromagnetic (TEM) mode, which is unique in that it has radial symmetry in the electric field distribution and a linear relationship between frequency and wave vector. This gives the TEM mode two exceptional properties. First, the radial symmetry implies that one need not worry about possible rotations of the polarization of the field after it passes through the waveguide. Second, the linear relationship ensures that a pulse of different frequencies will retain its shape as it propagates along the waveguide. The crucial disadvantage of a coaxial metallic waveguide is that it is useless at optical wavelengths because of heavy absorption losses in the metal. For this reason, optical waveguiding is restricted to the use of dielectric materials. However, because of the differences in boundary conditions of the electromagnetic fields at metal and dielectric surfaces, it has not previously been possible to recreate a TEM-like mode with all-dielectric materials. Consequently, optical waveguiding is done with the traditional index-guiding (that is, total internal reflection) mechanism, as exemplified by silica and chalcogenide optical fibers. Such dielectric waveguides can achieve very low losses (2). Although the

optical fiber has proven to be undeniably successful in many ways, it is nevertheless plagued by two fundamental problems. First, because the fundamental mode in the fiber has an electric field with twofold p-like symmetry, the polarization of light coming in one end of the fiber and the polarization coming out the other are generally completely different. This leads to substantial problems when coupling into polarization-dependent devices. Second, because the guiding involves total internal reflection, it is not possible for light to travel in a fiber with a sharp bend whose radius of curvature is less than 3 mm without significant scattering losses (3). For light at optical wavelengths, this is a comparatively enormous radius, thus limiting the scale of possible miniaturization.

Recently, however, all-dielectric waveguides have been introduced that confine optical light by means of one-dimensional (1D) (4) and 2D (5, 6) photonic bandgaps. Although single-mode propagation is still twofold p-like symmetric, these new designs have the potential advantage that light propagates mainly

through the empty core of a hollow waveguide (7), thus minimizing effects associated with material nonlinearities and absorption losses. Moreover, because confinement is provided by the presence of at least a partial photonic bandgap, this ensures that light should be able to be transmitted around a bend with a smaller radius of curvature than is possible with the optical fiber.

Here we introduce a waveguide, the coaxial omniguide, that combines some of the best features of the metallic coaxial cable and the dielectric waveguides. It is an all-dielectric coaxial waveguide and supports a fundamental mode that is very similar to the TEM mode of the metallic coaxial cable. It has a radially symmetric electric field distribution so that the polarization is maintained throughout propagation. It can be designed to be single-mode over a wide range of frequencies. In addition, the mode has a point of intrinsic zero dispersion around which a pulse can retain its shape during propagation, and this point of zero dispersion can be placed in the single-mode frequency window. Finally, the coaxial omniguide can be used to guide light around sharp bends whose radius of curvature can be as small as the wavelength of the light. This waveguide design is completely general and holds over a wide range of structural parameters, materials, and wavelengths. To our knowledge, this work represents the first successful attempt to bridge the disparate modal regimes of the metallic coaxial cable and the dielectric waveguides.

A cross section of a traditional metallic coaxial waveguide is shown in Fig. 1A. Light is confined in the radial direction in the region between the two metal cylinders and travels in the axial direction (perpendicular to the plane of the figure). In a simple ray model, propagation of light through the coaxial cable can be viewed as a result of successive specular reflections off the metal
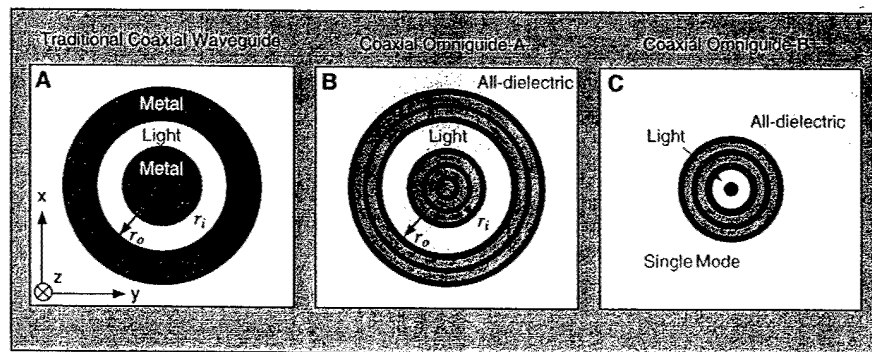

Fig. 1. Schematics of coaxial waveguide cross sections. **(A)** Traditional metallic coaxial cable. **(B and C)** Two embodiments, of type A and B, respectively, of the all-dielectric coaxial omniguide as described in the text. The blue cylindrical dielectric layers correspond to high dielectric constant material, and the green cylindrical dielectric layers correspond to low dielectric constant material. For all cases (A through C), light can be confined within the coaxial region (for example, $r_i < r < r_o$) and guided along the axial or z direction. In (A) and (B), $r_i = 3.00\ a$ and $r_o = 4.67\ a$, whereas in (C), $r_i = 0.40\ a$ and $r_o = 1.40\ a$.

[1]Center for Materials Science and Engineering and Department of Physics, Massachusetts Institute of Technology, Cambridge, MA 02139, USA. [2]Department of Materials Science and Engineering, Massachusetts Institute of Technology, Cambridge, MA 02139, USA.

walls. The dispersion relations for the first few modes supported by a metallic coaxial waveguide are shown in Fig. 2A. For definiteness, the inner and outer radii of the waveguiding region are taken to be $r_i = 3.00$ a and $r_o = 4.67\ a$, respectively, where a is an arbitrary unit of length to be defined later. For any value of the wave vector, the lowest frequency mode is the TEM mode for which both the electric and magnetic fields are transverse to the direction of propagation. This mode has zero angular momentum, which means that the mode is invariant under rotations around the axial direction. Another useful property of this mode is its constant group velocity, which makes it dispersionless at any frequency. The other modes shown in the plot are transverse electric (TE_{ml}) modes for $l = 1$ and varying angular momenta m (8). The cutoff frequency of any of these modes is of the form

$$\omega_{cutoff} = \frac{c}{r_o}\ f\left(\frac{r_o}{r_i}\right)$$

where f is the solution to a transcendental equation for each value of the angular momentum m and for each polarization (TE or TM) (1).

Designing an all-dielectric waveguide with similar principles of operation as the metallic coaxial waveguide is not straightfor-

ward, because the boundary conditions at a dielectric-dielectric interface differ from those at an air (dielectric)-metal interface. In particular, specular reflections cannot be obtained on a dielectric-dielectric interface when the ray of light comes from the region with a lower index of refraction. Thus, it has generally been assumed that an all-dielectric coaxial waveguide cannot be designed to support a TEM-like mode, even in principle. However, recent research on the omnidirectional dielectric reflector (9) has opened new possibilities for reflecting, confining, and guiding light with all-dielectric materials. Indeed, a dielectric hollow waveguide using this principle was recently fabricated and tested successfully at optical wavelengths (4). The omnidirectional dielectric reflector, or simply the dielectric mirror, is a periodic, multilayered planar structure consisting of alternating layers of low and high indices of refraction. This structure can be designed so that there is a range of frequencies at which incoming light from any direction and of any polarization is reflected. Moreover, the electric fields of the reflected light in this frequency range have corresponding phase shifts that are quite close to those acquired upon reflection from a metal. In fact, there is a frequency for each angle of incidence and each polarization, for which the phase shift is

identical to that of a metal. This observation, together with the fact that high reflectivity of the omnidirectional dielectric mirror is maintained for all angles of incidence, strongly suggests exploration of the possibilities of using an omnidirectional mirror in lieu of a metal in coaxial cable designs. In effect, the omnidirectional dielectric mirror provides a new mechanism for guiding optical and infrared light without incurring the inherent losses of a metal.

In a cross section of a coaxial waveguide (Fig. 1B), the metal cylinders from the left panel have been replaced with cylindrical dielectric layers (10) associated with an omnidirectional mirror. We call this particular coaxial waveguide embodiment coaxial omniguide A. The parameters of the dielectric layers are taken from the hollow waveguide experiment (4) to be the following: Layers shown in dark blue have an index of refraction $n_1 = 4.6$ and a thickness $d_1 = 0.33\ a$, whereas layers shown in green have $n_2 = 1.6$ and $d_2 = 0.67\ a$. Here, $a = d_1 + d_2$ is the unit length of periodicity of the multilayered structure. The inner (r_i) and outer (r_o) radii of the coaxial waveguiding region are taken to be the same as those of the metallic coaxial cable described earlier. For the calculations presented here, we have set the index of refraction of the coaxial waveguiding region
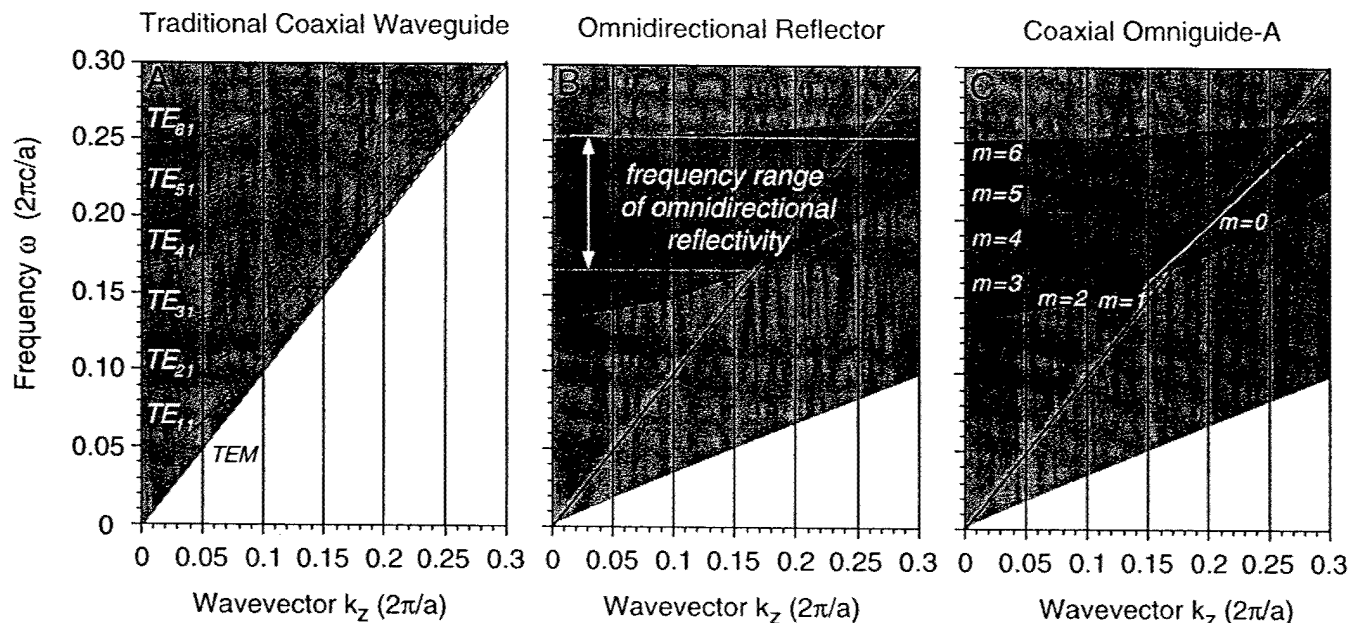
Traditional Coaxial Waveguide

Omnidirectional Reflector

Coaxial Omniguide-A

Fig. 2. Projected band structures along an axial direction. **(A)** Traditional metallic coaxial cable with inner and outer coaxial radii of $r_i = 3.00\ a$ and $r_o = 4.67\ a$, respectively. The red bands correspond to allowed guided modes. For any given wavevector, the lowest frequency mode is a TEM mode characterized by a perfectly linear dispersion relation. The six next highest bands correspond to transverse electric (TE_{ml}) modes with $l = 1$ and increasing angular momentum m. **(B)** Omnidirectional, reflecting, all-dielectric multilayer film. Light-blue regions correspond to modes for which light is allowed to propagate within the dielectric mirror, and dark-blue regions correspond to modes for which light is forbidden to propagate within the dielectric mirror. The diagonal black line identifies the edge of the light cone. The horizontal gray lines mark the boundaries in frequency within which omnidirectional reflectivity is possible. **(C)** Coaxial omniguide A with inner and outer coaxial radii of $r_i = 3.00\ a$ and $r_o = 4.67\ a$, respectively, and bilayers consisting of indexes of refraction $n_1 = 4.6$ and $n_2 = 1.6$ and thickness $d_1 = 0.33\ a$ and $d_2 = 0.67\ a$, respectively. The red and yellow bands indicate guided modes confined to the coaxial region of the waveguide. The dashed lines indicate modes with less than 20% localization within the coaxial region. There is close correspondence between the modes labeled $m = 1$ to $m = 6$ and those of (A) labeled TE_{11} to TE_{61}. Also, the yellow $m = 0$ mode corresponds to a TEM-like mode, as discussed in the text.

to be 1. In practice, in order to provide structural support, the coaxial waveguiding region may be chosen to be a dielectric with a low index of refraction without affecting the favorable properties of the coaxial omniguide (11).

Before we begin our investigation of the modes supported by the coaxial omniguide, it is instructive to first review the modes of a planar omnidirectional dielectric mirror. The projected band structure of the omnidirectional mirror is shown in Fig. 2B. The light blue regions represent allowed propagation modes of light within the dielectric mirror. The dark blue region represents modes for which light is forbidden to propagate within the dielectric mirror. The thick black line identifies the edge of the light cone, and the horizontal gray lines demarcate the frequency range of omnidirectional reflectivity. It is precisely within this range of frequencies that one would expect the coaxial omniguide to support modes that are most reminiscent of those of the metallic coaxial cable. To calculate the frequencies and field patterns of the modes of coaxial omniguide A, we proceed as described below.

As a result of the cylindrical symmetry of the system, there are two good "conserved quantities" that can be used to specify and classify the various modes supported by this waveguide. These are k_z, the axial component of the wave vector, and m, the angular momentum ($m = 0, 1, 2 \ldots$). For a given mode, the radial and angular components of the electric and magnetic fields can be calculated from the corresponding z (axial) components (12). For a given wave vector k_z and angular momentum m, the axial field components in a layer of index n have the general form

$$F(z,r,\phi) = [AJ_m(k_T r) + BY_m(k_T r)]$$
$$\times (C_1 e^{im\phi} + C_2 e^{-im\phi})e^{i(\omega t - k_z z)} \quad (1)$$

where F stands for either E_z or H_z; J_m and Y_m are Bessel functions (13) of the first and second kind, respectively; and k_T is a transverse wave vector $k_T = \sqrt{(n\omega/c)^2 - k_z^2}$.

The modes of the coaxial omniguide are calculated with two different approaches. The first is a semianalytic approach based on the transfer matrix method (14). Starting from Maxwell's equations, the z components of the electric and magnetic fields in each layer can be written in the general form given by Eq. 1. For given k_z, ω, and m, the only variables that determine the E_z and H_z fields are the four coefficients in front of the Bessel functions (two for E_z and two for H_z). The boundary conditions at the interfaces between adjacent layers can be written in the form of a matrix equation

$$\begin{pmatrix} A \\ B \\ A' \\ B' \end{pmatrix}_{j+1} = M \begin{pmatrix} A \\ B \\ A' \\ B' \end{pmatrix}_j \quad (2)$$

where $\begin{pmatrix} A \\ B \\ A' \\ B' \end{pmatrix}_j$ are the coefficients that determine the electric and magnetic fields in the jth layer, and M is a 4-by-4 transfer matrix that depends on k_z, ω, m, the geometry of the layers, and their indices of refraction. After calculating the electromagnetic fields for a given point (k_z, ω), we find the resonant modes by examining the fractional E-field power confinement in the coaxial waveguiding region; that is

$$\int_{r_i < r < r_o} dr\varepsilon(r)|E(r)|^2\omega / \int_{\text{all layers}} dr\varepsilon(r)|E(r)|^2\omega$$

$$(3)$$

The second approach involves a numerical solution of Maxwell's equations in the frequency domain with the use of the conjugate gradient method within the supercell approximation (15). Supercells of size (30 a by 30 a by 0.1 a) were used, leading to a basis set of about 230,000 plane waves. Eigenvalues were considered converged when the residue was less than 10^{-6}. The results of both approaches were found to agree to better than 0.1%.

In the projected band structure for coaxial omniguide A (Fig. 2C), the red and yellow bands represent guided modes localized within the region defined by the inner and outer coaxial radii of the waveguide. The dashed lines represent modes with less than 20% localization within the coaxial region. There is close correspondence between the modes within the omnidirectional reflectivity range labeled $m = 1$ to $m = 6$ and those of the coaxial cable labeled TE_{11} to TE_{61} (16). The $m = 0$ mode appears to correspond to the TEM mode. Of course, for a coaxial omniguide with a limited number of outer shells, these modes can only exist as resonances. Nevertheless, even with only 2.5 bilayers, we find that they can be extremely well localized resonances, and the leakage rate decreases exponentially with the number of shells. The strong localization is shown in Fig. 3. Here, we plot the power density in the electric field for the four lowest frequency modes at $k_z = 0.19 (2\pi/a)$. As the color bar indicates, power increases in going from black to dark red, to red, to orange, to yellow. The blue circles identify the boundaries between the various dielectric shells and are included as a guide to the eye. In all cases, the power is confined primarily within the coaxial region. This is particularly true for the $m = 0$ mode, which is also cylindrically symmetric, just like the TEM mode. Although it is well known that a waveguide consisting only of dielectric material cannot support a true TEM mode (17),
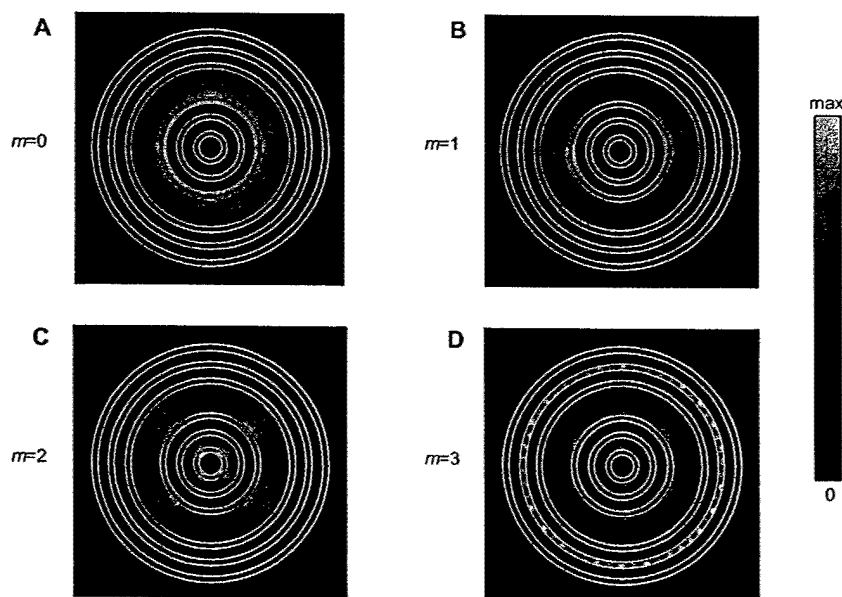

Fig. 3. Power density in the electric field for guided modes at $k_z = 0.19 (2\pi/a)$ in Fig. 2C. (A through D) correspond to guided modes with angular momenta $m = 0$ to $m = 3$, respectively. The color bar indicates that power increases in going from black to dark red, to red, to orange, to yellow. The blue circles identify the boundaries between the various dielectric shells and are included as a guide to the eye. Most of the power is confined to the coaxial region of the waveguide. The cylindrical symmetry and radial dependence of the $m = 0$ mode are consistent with those of a TEM mode. [The small fluctuations in density away from perfect cylindrical symmetry in (A) are a consequence of the discrete cubic grid used in the computations.]

we find that the $m = 0$ mode (which is a pure TM mode) possesses several of the characteristics of the TEM mode. First, as mentioned above, it has zero angular momentum and hence a radially symmetric electric field distribution. Second, the electric and magnetic fields within the coaxial waveguiding region (where over 65% of the power is concentrated) are nearly identical to those of the metallic coaxial cable; for example, the predominant components are E_r and H_f and vary as $1/r$. Finally, at the point where the $m = 0$ dispersion curve (yellow line) crosses the light line, there is an exact correspondence between the electromagnetic fields of the coaxial omniguide and the metallic coaxial cable, inside the coaxial region. Moreover, the derivative of the group velocity is exactly zero near this point, leading to nearly dispersionless propagation throughout its vicinity (18).

The characteristics described above are certainly the attributes one would hope to achieve in order to overcome problems with polarization-rotation and pulse broadening. But what about single-mode behavior? The bands shown in Fig. 2C are clearly multimode; that is, for a given frequency there are two or more guided modes that can be excited. To design a coaxial omniguide that can support single-mode behavior, we need only readjust our structural parameters. It is easier to keep the parameters of the bilayers fixed, so that the omnidirectional re-

flectivity frequency range does not change. This leaves only those parameters that are common to both the coaxial omniguide and the metallic coaxial cable: the inner and outer radii of the coaxial waveguiding region. Single-mode operation for the TEM-like mode will only be possible if all other modes are moved up in frequency so that the lowest nonzero angular mode has its cutoff frequency inside the bandgap. To do this, we have to decrease the inner radius of the coaxial waveguiding region. At the same time, the thickness of the bilayers, a, should remain constant, which means that we can no longer accommodate three bilayers in the inner part of the waveguide. Actually, the inner radius has to be decreased so much that we are forced to discard the periodic structure in the inner region and to replace it with a single dielectric rod. Loss of the inner-core mirror structure is not crucial, however. What is important is to add a thin rod of dielectric in the core in order to avoid the $1/r$ divergence of the field at the origin and to use a dielectric of high enough contrast to localize the TEM-like mode in the coaxial region. This approach, however, will not work if $r_i > a$, and one must then revert to a multilayer core. Testing different values for the inner and outer radii of the waveguiding region, we have found a configuration that has the desired properties. This new embodiment, coaxial omniguide B, is shown in Fig. 1C. The central dielectric rod has an index of refraction $n_1 = 4.6$ and a radius $r_i = 0.40\ a$. The coaxial waveguiding region has an outer radius $r_o = 1.40\ a$, and the parameters of the outer bilayers are the same as those used for configuration A. In configuration B, there are two frequency ranges where the waveguide can operate in a single-mode fashion. We plot the dispersion curves for the modes supported by coaxial omniguide B in Fig. 4. The yellow dots indicate more than 50% confinement of the electric field power, whereas the red dots represent confine-

ment between 20 and 50%. (The dashed lines indicate confinement that is less than 20%.) The two white boxes identify the frequency ranges where the $m = 0$ band is single-mode. A comparison of Figs. 2C and 4 reveals that the cutoff frequency of the $m = 1$ band has shifted significantly upward, whereas the $m = 0$ band remains relatively unchanged. The flatness of the $m = 1$ band (19) enables the TEM-like band to be single-mode both above it and below it in frequency. The exact values of the parameters were chosen so that, in the middle of the higher frequency single-mode window [at $\omega = 0.205$ $(2\pi c/a)$], the mode is also dispersionless (18).

Figure 5 shows the distribution of the electric field components for the $m = 0$ mode of coaxial omniguide B at $k_z = 0.2\ (2\pi/a)$ and $\omega = 0.203\ (2\pi c/a)$. Because the (k_z, ω) point is very close to the light line, the electric field in the waveguiding region is almost completely transverse to the direction of propagation. (The z component of the magnetic field will always be zero because this is a pure TM mode.) The field distribution clearly reveals a high confinement of the mode in the waveguiding region, as desired. Moreover, these values of E_x and E_y lead to a net field distribution that is completely radially symmetric, consistent with an angular component that is exactly zero. All the features mentioned above attest to the close correspondence between the $m = 0$ mode and a pure TEM mode.

There are several additional issues associated with the coaxial omniguide. The first is a practical issue involving the coupling of light into the coaxial omniguide. One possible method for coupling would be to begin with an omniguide with a very thin core that increases gradually to match the core of the coaxial configuration. Because the electromagnetic field of a laser source can have a TEM_{00} mode, this should lead to efficient coupling into the TEM-
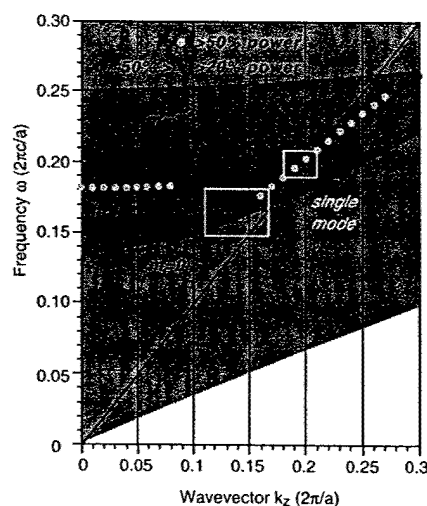

Fig. 4. Projected band structure for coaxial omniguide B. The central dielectric rod has an index of refraction $n_1 = 4.6$ and a radius $r_i = 0.40\ a$. The coaxial waveguiding region has an outer radius $r_o = 1.40\ a$, and the parameters of the outer bilayers are the same as those used for configuration A. The yellow dots represent confinement of the electric field power of more than 50%; the red dots represent confinement between 20 and 50%; and the dashed lines represent confinement less than 20%. The two white boxes identify the frequency ranges where the $m = 0$ band exhibits single-mode behavior.
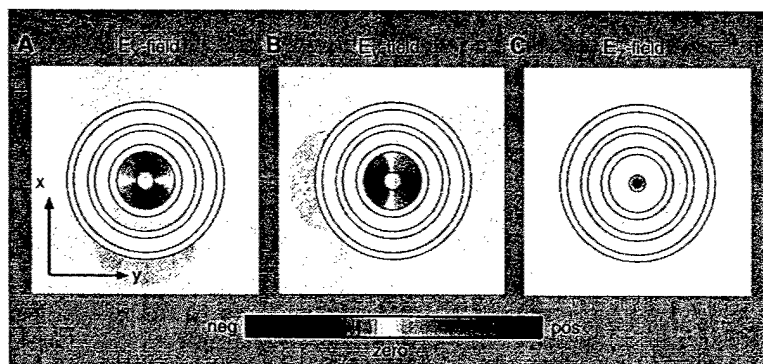

Fig. 5. Electric field for the mode at frequency 0.203 $(2\pi c/a)$ and $k_z = 0.2\ (2\pi/a)$ in Fig. 4. (A through C) Electric field components along the x, y, and z directions, respectively. The color bar indicates that large positive and negative values are shown as dark red and dark blue regions, respectively, whereas white areas represent regions of zero values of the electric field, and light-colored areas represent regions of low values of the electric field. The field distribution clearly reveals a high confinement of the mode in the coaxial waveguiding region, and in this region it is nearly completely transverse to the direction of propagation (less than 10^{-3} of the intensity is along z), as desired.

like mode of the coaxial omniguide. The second issue concerns the ability to transmit information across a broad band of frequencies with the coaxial omniguide. This is determined primarily by the width of the omnidirectional reflectivity range. Another issue is that the multitude of adjustable parameters in the structure of a coaxial omniguide (the index of refraction and thickness of each layer, the thickness of a bilayer, the waveguiding region inner and outer radii, the central rod index of refraction, and so on) allows for great flexibility in tuning the waveguide for optimal desired performance (confinement in the waveguiding region, width of single-mode window, frequency of zero dispersion, group velocity, and so on). A further important issue is that radial confinement of the light is a consequence of omnidirectional reflection and not of total internal reflection. This means that the coaxial omniguide can be used to transmit light around much sharper corners than is possible with the optical fiber. Finally, the radial decay of the electromagnetic field in the coaxial omniguide is much faster than in the case of the optical fiber (with only 10 bilayers, one gets a decrease of electric field intensity of about six orders of magnitude). This means that, for guided light of the same wavelength, the outer diameter of the coaxial omniguide can be much smaller than the diameter of the cladding layer of the optical fiber without leading to cross-talk complications in waveguide bundles. These enabling characteristics of a substantially smaller waveguide bending radius and smaller spacing of adjacent waveguides lead to the possibility of substantial miniaturization of future integrated optical devices and transmission lines.

References and Notes

1. R. A. Waldron, *Theory of Guided Electromagnetic Waves* (Van Nostrand Reinhold, London, 1969).
2. B. E. A. Saleh and M. C. Teich, *Fundamentals of Photonics* (Wiley, New York, 1991).
3. See, for example, S. E. Miller and A. G. Chynoweth, Eds., *Optical Fiber Telecommunications* (Academic Press, New York, 1979).
4. Y. Fink et al., *J. Lightwave Technol.* 17, 2039 (1999).
5. J. C. Knight et al., *Science* 282, 1476 (1998).
6. R. F. Cregan et al., *Science* 285, 1537 (1999).
7. The first attempts at hollow waveguides in the optical regime actually involved metallodielectric materials. See, for example, M. Miyagi et al., *Appl. Phys. Lett.* 43, 430 (1983), and Y. Matsuura and J. Harrington, *J. Opt. Soc. Am.* 14, 6 (1997), and references therein.
8. The waveguide also supports transverse magnetic (TM) modes, but they do not appear in the plot because the cutoff frequency for the lowest lying TM mode is larger than 0.30 $(2\pi c/a)$.
9. Y. Fink et al., *Science* 282, 1679 (1998).
10. The idea of radially confining light by means of a dielectric multilayer structure was first investigated by P. Yeh et al. (*14*). Our work differs in that our waveguide is coaxial, and the multilayer film is chosen so that there exists a frequency range of omnidirectional reflectivity. Both of these properties are important in order to create a TEM-like mode.
11. For example, setting the index of refraction of the coaxial waveguiding region to 1.3 (instead of 1.0), with $n_1 = 4.6$ and $n_2 = 1.8$, the original omnidirectional reflectivity frequency range of 0.17 to 0.25
12. A. Yariv, *Optical Electronics in Modern Communications* (Oxford Univ. Press, New York, 1997).
13. C. J. Tranter, *Bessel Functions with Some Physical Applications* (Hart, New York, 1969).
14. P. Yeh, A. Yariv, E. Marom, *J. Opt. Soc. Am.* 68, 1196 (1978).
15. R. D. Meade et al., *Phys. Rev. B* 77, 8434 (1993); erratum: *Phys. Rev. B* 55, 15942 (1997).
16. The small discontinuity in $m = 2$ arises from a weak coupling to a resonant mode of the same symmetry localized deep within the core region.
17. N. J. Cronin, *Microwave and Optical Waveguides* (Institute of Physics, Bristol, UK, 1995).
18. For simplicity, we only consider the intrinsic waveguide dispersion in all our calculations. In a real waveguide, we

$(2\pi c/a)$ in Fig. 2B reduces to a range of 0.18 to 0.23 $(2\pi c/a)$, whereas the modal structure shown in Fig. 2C remains essentially unaltered.

would also have material dispersion, which can be compensated for in the standard manner by judicious tuning of the waveguide parameters. Indeed, the multitude of available parameters for the coaxial omniguide provides a much greater flexibility to accomplish this than in the case of an optical fiber.
19. We find that the very small group velocity exhibited by the $m = 1$ mode can be driven even to negative values with a proper choice of waveguide parameters.
20. We thank S. Johnson for many helpful discussions. Supported in part by the U.S. Army Research Office under grant DAAG55-97-1-0366, by the Materials Research Science and Engineering Center of NSF under award DMR-9808941, and by the U.S. Department of Energy under grant DE-FG02-99ER45778.

Holes in a Quantum Spin Liquid

Guangyong Xu,[1] G. Aeppli,[2] M. E. Bisher,[2] C. Broholm,[1,3]*
J. F. DiTusa,[4] C. D. Frost,[5] T. Ito,[6] K. Oka,[6] R. L. Paul,[3]
H. Takagi,[7] M. M. J. Treacy[2]

Magnetic neutron scattering provides evidence for nucleation of antiferromagnetic droplets around impurities in a doped nickel oxide–based quantum magnet. The undoped parent compound contains a spin liquid with a cooperative singlet ground state and a gap in the magnetic excitation spectrum. Calcium doping creates excitations below the gap with an incommensurate structure factor. We show that weakly interacting antiferromagnetic droplets with a central phase shift of π and a size controlled by the correlation length of the quantum liquid can account for the data. The experiment provides a quantitative impression of the magnetic polarization cloud associated with holes in a doped transition metal oxide.

Spin density modulations in transition metal oxides are receiving huge attention because of possible connections to high-temperature superconductivity. The modulations appear upon introduction of charge carriers, through chemical substitution, into an insulating and antiferromagnetic parent compound and tend to be static when the carriers are frozen and dynamic when they are mobile. Evidence for such modulations has been largely confined to materials whose magnetism and charge transport are quasi–two-dimensional (*1–4*) and whose parent insulators are ordered antiferromagnets. We provide evidence for analogous phenomena in a quasi–one-dimensional oxide (*5*), $Y_{2-x}Ca_xBaNiO_5$, for which the parent is a spin liquid by virtue of quantum

[1]Department of Physics and Astronomy, Johns Hopkins University, Baltimore, MD 21218, USA. [2]NEC Research Institute, 4 Independence Way, Princeton, NJ 08540, USA. [3]National Institute of Standards and Technology Center for Neutron Research, Gaithersburg, MD 20899, USA. [4]Department of Physics and Astronomy, Louisiana State University, Baton Rouge, LA 70803, USA. [5]ISIS Facility, Rutherford Appleton Laboratory, Chilton, Didcot, Oxon OX11 0QX, UK. [6]Electrotechnical Laboratory, Tsukuba 305, Japan. [7]Department of Advanced Materials Science, Graduate School of Frontier Sciences, University of Tokyo Hongo, Tokyo 113-8656, Japan.

*To whom correspondence should be addressed. E-mail: broholm@jhu.edu

fluctuations (*6–10*) and which has motivated considerable theoretical activity (*11–16*).

The key features of this orthorhombic material are the chains of NiO_6 octahedra (Fig. 1A). The octahedra are corner-sharing, which results in the dominance of magnetism (*8*) and electrical conduction (*5*) by the very simple ..O-Ni-O-Ni-O.. backbone. The magnetic degree of freedom at each Ni site is the spin $S = 1$ associated with the $3d^8$ configuration of Ni^{2+}. Each of the $S = 1$ ions is coupled to its neighbors through antiferromagnetic (AFM) superexchange through shared O^{2-} ions. Replacing the off-chain Y^{3+} by Ca^{2+} introduces holes primarily onto apical oxygen atoms in the chains, and while the materials remain insulators, doping substantially increases conductivity at finite temperatures. Thus, $Y_{2-x}Ca_xBaNiO_5$ is a one-dimensional analog of the cuprates, where off–CuO_2-plane chemical impurities donate holes to the CuO_2 planes.

Magnetic one-dimensionality causes the parent compound Y_2BaNiO_5 to be a spin liquid prevented from ordering antiferromagnetically by quantum fluctuations. The material is not an ordinary paramagnet with heavily damped spin fluctuations, but rather the magnetic analog of superfluid ^{4}He because it has a macroscopically coherent quantum